



CONSTRUCTED FACILITIES CENTER



PB98-140684

UTILIZATION OF THE SIMULATION
METHOD TO EVALUATE
INFRARED THERMOGRAPHY
Contract No. T699-CIDDMOC Subtask-A4
CFC 95-219

Darrell R. Dean, Jr., Ph.D., P.S.
Yiming Hu

Submitted to:

West Virginia Department of Transportation
Division of Highways
1900 Kanawha Blvd. East
Charleston, WV 25305-0430

September 1995

*College of Engineering and
Mineral Resources
West Virginia University*

1. Report No. CFC95-219	2. Government Accession No.	3. Recipient's Catalog No.	
4. Title and Subtitle Utilization of the Simulation Method to Evaluate Infrared Thermography		5. Report Date 9/29/95	
		6. Performing Organization Code OSP#88-409	
7. Author(s) Darrell R. Dean, Jr Yiming Hu		8. Performing Organization Report No. CFC95-219	
9. Performing Organization Name and Address Constructed Facilities Center West Virginia University P.O. Box 6103 Morgantown, WV 26506-6103		10. Work Unit No. (TRAIS)	
		11. Contract or Grant No. T-699 CDDMOC-Subtask A-4	
12. Sponsoring Agency Name and Address West Virginia Division of Highway 1900 Kanawha Blvd., East, Building Five Charleston, WV 25305-0430		13. Type of Report and Period Covered Final 11/9/88 to 9/30/95	
		14. Sponsoring Agency Code	
15. Supplementary Notes			
16. Abstract <p>Infrared thermography as a remote sensing technique for pavement defect detection is a relatively new technology and is still under research, although there have been several studies and practical applications of this technique on bridge decks, airport runway surfaces, and pavements. In this study, a simulation method was developed to investigate the infrared thermography for highway pavement evaluation. Through the consideration of factors such as camera height, tilt angle, pixel size, and the criteria for classifying boundary pixels, simulated pavement images were generated with a simulation program. The results of the data analysis are:</p> <ol style="list-style-type: none"> 1. The effect of camera height is not significant or the height is independent of the radiation heat energy based on the theoretical energy transfer model. So a higher camera height may be used to acquire images. By adopting a higher camera height, larger pavement areas can be scanned and evaluated with no significant loss of accuracy. 2. The effect of the camera tilt angle is significant and this effect is affected by the position of the crack area in the image frame. 3. The effect of the pixel size is significant. The smaller the pixel size, the higher the spacial resolution and the better the image quality. 4. The effect of the criterion used to classify the boundary pixels is significant. So when using software to deal with the infrared thermography, the criterion to classify boundary pixels as either sound or crack pixels should be considered carefully to get a good offset to the accuracy loss. 			
17. Key Words Infrared, simulation, camera geometry, thermogram.		18. Distribution Statement	
19. Security Classif. (of this report) Unclassified	20. Security Classif. (of this page) Unclassified	21. No. of Pages 99	22. Price

DISCLAIMER

"The contents of this report reflect the views of the author who is responsible for the facts and the accuracy of the data presented herein. The contents of this report do not reflect the official views or policies of the West Virginia Department of Transportation."

TABLE OF CONTENTS

ACKNOWLEDGEMENTS	i
TABLE OF CONTENTS	ii
LIST OF TABLES	iv
LIST OF FIGURES	v
LIST OF EQUATIONS	vii
 CHAPTER I INTRODUCTION	 1
Background	1
Problem Statement	3
Evaluation Methods of Infrared Thermography	6
Objective	8
Organization of Thesis	9
 CHAPTER II LITERATURE REVIEW	 10
Principle of Infrared Thermography	10
Case Histories	11
Advantages and Disadvantages	14
Image processing system	15
 CHAPTER III COMPONENTS OF THE SIMULATION MODEL	 17
Thermal Components	17
General radiation heat transfer model	17
Determination of the infrared fraction of the	
emissive power (E)	20
Modeling of defective pavement with V-shaped cracks ..	23
The emissive power (E)	23
Solution to emissive power calculation	25
Camera Component	31
Geometric Component of the Model	32
Coordinate system	32
Collinearity equations	36
Finite area ($\Delta s'$ and Δs)	41
Length components	42
Angles ($\cos(\phi)$ and $\cos(\phi')$)	43
The simulated concrete test specimen	46

CHAPTER IV	PROCEDURE FOR DEVELOPING THE	
	SIMULATION MODEL	48
Simulation Program		48
Sample pavement area projection onto sensor plane		48
Radiative heat energy calculation for sound		
pavement element		48
Crack band projection		50
Boundary pixel classification		52
Location of the boundary pixels		52
Classification of the boundary pixel		55
Crack pixel Identification and Creation of Crack file		59
Calculation of the Crack Percentage		63
CHAPTER V	RESULTS AND ANALYSIS	64
Simulated Data Summary		64
Analysis of the Results		71
Camera geometry (camera height and tilt angle)		71
Crack percentage independent of camera height		78
Image location on the sensor plane		81
Pixel size		84
The criterion of classifying the boundary pixels		84
CHAPTER VI	SUMMARY, CONCLUSIONS AND	
	RECOMMENDATIONS	86
Summary		86
Conclusions		87
Recommendations		88
REFERENCE		90
APPENDIX. Blackbody Emissive Power Table		94

LIST OF TABLES

TABLE 1.	Small area (3.26' by 3.26'), H = 6', control crack = 7.03%	65
TABLE 2.	Small area (3.26' by 3.26'), H = 8', control crack = 7.03%	66
TABLE 3.	large area (5.42' by 5.42'), H = 10', control crack = 11.49%	67
TABLE 4.	Crack percentage at the designed image frame (control crack = 6.0%)	82

LIST OF FIGURES

Figure 1. Components of automated inspection system	5
Figure 2. Digital image	6
Figure 3. Graphical interpretation of Lambert's law	18
Figure 4. Energy exchange between two surface elements	19
Figure 5. V-shaped crack	24
Figure 6. Emissive power of the V-shaped crack with vertex angle 60°	28
Figure 7. Emissive power of the V-shaped crack with vertex angle 45°	29
Figure 8. Emissive power of the V-shaped crack with vertex angle 30°	30
Figure 9. Coordinate system on the sensor plane	32
Figure 10. The camera scanning a pavement system	33
Figure 11. Object and image coordinate system	34
Figure 12. Relationship between pixel and its projected area	42
Figure 13. Projective relationship and spatial length and angles	43
Figure 14. Angle between a line and a plane	44
Figure 14.1 Simulated sample areas	47
Figure 15. Program block diagram	49
Figure 16. Image size and camera tilt angle	50
Figure 17. Images of crack bands as projected onto the sensor plane	51
Figure 18. Boundary pixel location	53
Figure 19. Boundary pixel location	55
Figure 20. The components of boundary pixel	57
Figure 21. The crack pixel location	59
Figure 22. The types of beginning-line and ending-line crack boundaries	61

Figure 23. Crack percentage as a function of tilt angle (pixel size = 0.02 mm)	68
Figure 24. Crack percentage as a function of tilt angle (pixel size = 0.04 mm)	69
Figure 25. Crack percentage as a function of tilt angle (pixel size = 0.06 mm)	70
Figure 26. Crack percentage with certain pixel size and same criterion . . .	72
Figure 27. The definition of h and Δ	73
Figure 28. Relative crack percentage as a function of tilt angle (pixel size = 0.02 mm)	75
Figure 29. Relative crack percentage as a function of tilt angle (pixel size = 0.04 mm)	76
Figure 30. Relative crack percentage as a function of tilt angle (pixel size = 0.06 mm)	77
Figure 31. Designed crack in the image frame	81
Figure 32. Crack percentage as a function of image location	83

LIST OF EQUATIONS

Equation 1.1 Lambert's law	17
Equation 1.2 Energy value	18
Equation 1.3 Solid angle	18
Equation 1.4 Energy value	18
Equation 2 Radiative intensity	19
Equation 3 Emissive power	19
Equation 4 Energy value (differential)	20
Equation 5 Energy value	20
Equation 6 Fraction of Emissive power	21
Equation 7 Linear equation of Q and B	22
Equation 8 Linear equation of Q and B	23
Equation 9 Emissive power of V-shaped crack	23
Equation 10 Emissive power of V-shaped crack (unitless)	25
Equation 11 Solution for (E)	27
Equation 12 Coordination system transfer	35
Equation 13 Coordination system transfer	35
Equation 14 Rotation matrix	36
Equation 15 Collinear function in vector form	36
Equation 16 Vector a	37
Equation 17 Vector A	37
Equation 18 Vector a to vector A with rotation matrix M	37
Equation 19 Vector a to vector A with rotation matrix M	37
Equation 20 Vector A to vector a with rotation matrix M	38

Equation 21 Vector A to vector a with rotation matrix M	38
Equation 22 Matrix form of equation 19	39
Equation 23 Expansion of equation 22	39
Equation 24 Collinearity equation without scale factor k	39
Equation 25 Collinearity equation (from image system to object system)	40
Equation 26 Collinearity equation (from object system to image system)	40
Equation 27 Collinearity equation (from object system to image system)	41
Equation 28 Finite element area	42
Equation 29 Length	42
Equation 30 $\cos(\phi)$	43
Equation 31 $\sin(\psi)$	43
Equation 32 $\cos(\phi')$	44
Equation 33 Linear equation (3D)	44
Equation 34 Linear equation (3D)	45
Equation 35 $\cos(\phi')$	45
Equation 36 Ratio of energy (total)	56
Equation 37 Energy ratio	56
Equation 38 Energy on crack area	57
Equation 39 Energy on sound area	57
Equation 40 Boundary energy	58
Equation 41 Ratio of energy (boundary and sound area)	58

CHAPTER I. INTRODUCTION.

Background

Well-designed and well-maintained pavements are essential for the safe and efficient movement of people, goods and services over ground transportation facilities. Computer-based Pavement Management Systems (PMS) include large databases of information that are used to make pavement repair and rehabilitation decisions (Carmichael, 1990, Schoenberger, 1984, and Uzarski, 1984). In addition to serving immediate maintenance needs, a PMS also allows the analysis of a pavement's performance over its lifetime. Such performance information can be used in making future pavement design decisions (Brown, 1990 and Clarke, et. al., 1990).

The quality of the pavement repair and rehabilitation decisions made with the assistance of a PMS is highest when the data it analyzes is current and accurate (Conner, 1990 and Kilaeski, 1990). Surface evaluation data is key when judging the service adequacy of a pavement (Darter, 1990 and Ritchie, et. al., 1986). Using a PMS, the maintenance engineer combines surface distress evaluations with other information to determine if further structural evaluation is necessary to determine the probable causes of the surface distress and to estimate the needs and priorities for preventative and corrective maintenance.

Distress surveys have been traditionally performed by raters who travel along the road and classify the distresses based on their visual observations. The distresses are recorded on data forms and the information is later reduced in the office. This type of manual procedure is slow, labor-intensive, and subject to

transcription errors. Consistency between classification and quantification of the distresses can also be a problem. There are other problems with manual data collection. When vehicular traffic cannot be totally excluded, conditions can be unsafe for the raters. Also, such procedures suffer from a high degree of subjectivity, proneness to error, and non-repeatability. The safety problem has been addressed by placing the inspection personnel in vehicles that move slowly along the pavement (Kilareski and Cumberledge, 1990), but the subjectivity issue still remains: ratings are not repeatable, both for the case where the same person rates the pavement under different conditions and the case where different people rate the pavement under similar conditions (Hill, 1990) and (Sime and Larsen, 1990). This subjectivity has two causes. People are fundamentally not capable of sustained peak performance when doing boring, repetitive inspection tasks. They are also not naturally capable of making quantitative visual measurements so they are asked to use qualitative pavement ratings. That is, instead of recording existing details about crack location, orientation, and size, they assess the severity (inconsequential, significant, bad) and extent (isolated, frequent) of the distress to determine pavement scores. Because of this subjectivity, differences persist, even when the personnel have been carefully trained (Copp, 1990 and Dankbar, 1990). Thus, there is a need for fast, objective pavement surface distress data collection systems. Automation is a solution to this need. Recent developments in electronic instrumentation and computer technology can be utilized to achieve automation.

In concept, automated pavement evaluation is straightforward. As a survey vehicle travels along the pavement, one or more cameras acquire images of the entire pavement surface. The images are either recorded on videotape or

photographic film for later analysis. A computer examines each image, locates cracks and other indicators of distress, characterizes the distress severity and extent, and reports the results in a form that can be stored in a PMS and interpreted by a pavement maintenance engineer.

In practice, one of the automated pavement evaluation systems utilizes infrared thermography which is a non-destructive remote means of measuring the surface temperature of an object. In general, the greater the temperature differential between the sound pavement and defective area, the easier it is to detect the distressed area. This temperature differential can be detected by a sensitive infrared scanner and then this information can be recorded on videotapes. These thermal images can be brought back to the laboratory for digital image processing and analysis.

Problem Statement

Although there have been several studies and practical applications of this pavement evaluation technology on bridge decks, highway pavements, and airport pavement surfaces, the application of infrared thermography to highway pavement evaluation has not received a lot of attention. Infrared thermography, as an automated pavement evaluation technology, should be capable of detecting the pavement surface condition rapidly, accurately, and reliably. This capability can be achieved under the proper conditions. These conditions include: 1) a high quality image from a properly calibrated and oriented camera, 2) an image free of noise due to weather conditions and non-defect stains such as tire marks and oil stains, and 3) optimum data processing.

In a study by Dean and Kadir (1992), it was found that the relationship between camera geometry and the ability to detect pavement cracks was contrary to conventional wisdom. Camera geometry in this work means camera tilt angle and camera height. The 1992 study by Dean and Kadir found that the ability to detect pavement cracks was independent of camera height. In addition, the optimum tilt angle for detecting pavement cracks was a tilt angle other than a zero tilt angle. All these conclusions were based on field tests. The field test method, however, has some limitations such as the effect of environmental factors. The image data acquired during the field test involves both the effects of camera geometry and the environmental factors. It makes the image data analysis difficult. So it is useful in the image data analysis to find some method which can isolate camera geometry from the environmental factors. One possible method is the simulation method which models the infrared thermography to create the image data. In the simulation method the environmental factors can be controlled. Therefore, this research focuses on the effects of infrared camera geometry and digital image processing on the ability to detect crack defects in highway pavements. The method of evaluating infrared thermography in this research is the simulation method. The basic concept of this method is to simulate the equipment function based on the simple radiative heat transfer theory and principles.

Like other inspection systems, infrared thermography systems involve four steps as shown in Figure 1. The function of the first two blocks is to capture the analogue signal of the image and convert it to a digital image. The function of the last two blocks is data processing and interpretation.

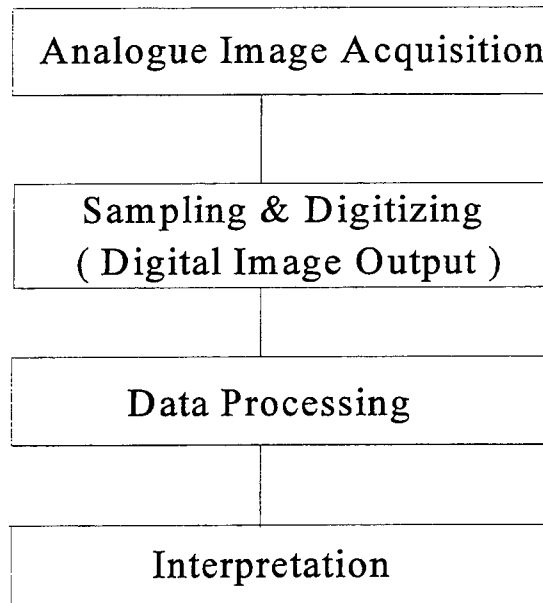


Figure 1. Components of automated inspection system.

As can be seen in Figure 2, a digital image is composed of numerical values. Usually, a digital image is stored as a computer file. If this file is displayed on a computer screen or printed out on paper, only numbers will be seen. So if we use a computer to create the digital data which are the same as the digital image data, and then use the created digital data instead of the real digital image data for data processing, the result is the same. The key to creating such a digital image is to find or build a model. The model must simulate the optical and thermal sensing function of a camera. With the model, a simulated pavement image may be created. Using this simulated image instead of the real pavement image for data analysis, the crack percentage can be calculated and the effect of camera geometry on the determination of the crack percentage can be analyzed. This is why the simulation method can be used to investigate the

application of infrared thermography to crack detection in highway pavements.

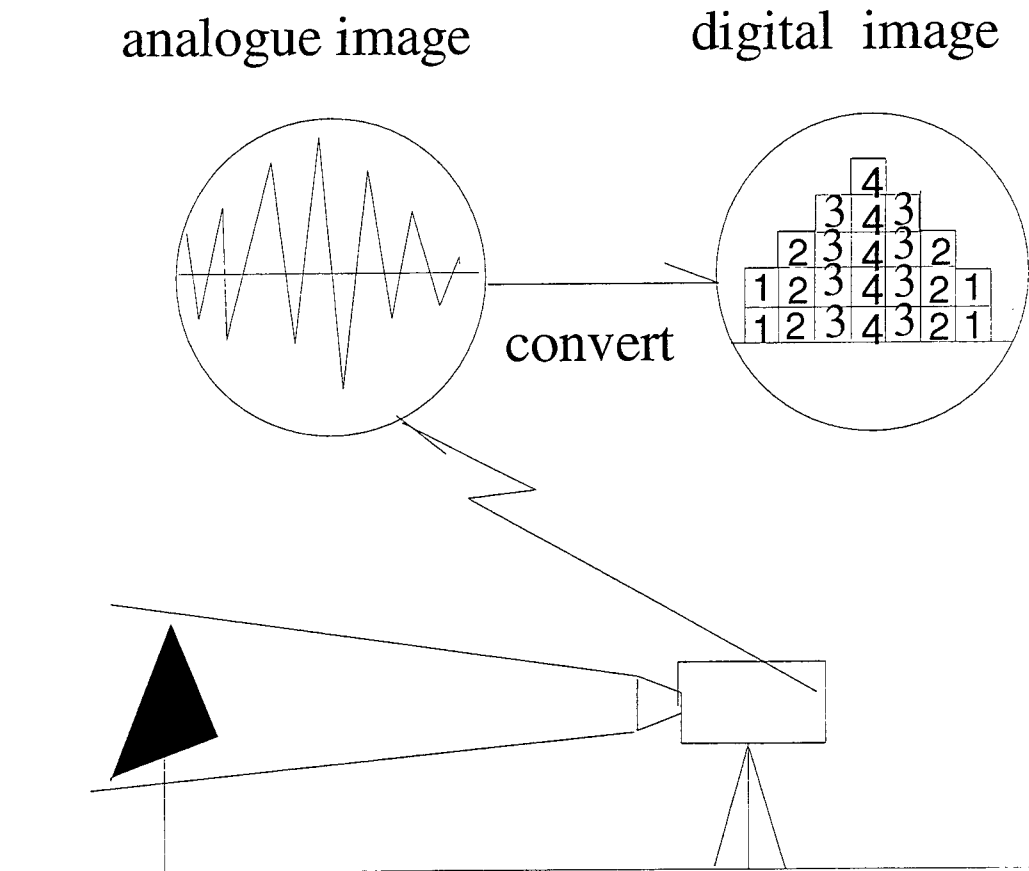


Figure 2. Digital image.

Evaluation Methods of Infrared Thermography

Three methods may be used to study and evaluate pavement inspection techniques. The methods are: field assessments via pilot studies, experimental methods, and simulation methods.

The procedure during a pilot study is to select a particular method or equipment, perform the survey or collect the appropriate data on a chosen route, process the resulting data, and compare the results with a conventional method or with other procedures on the same route. For example, Manning and Holt (1986) conducted a technical evaluation of various methods for evaluating the deterioration of asphalt-covered bridge decks. The methods evaluated were chain drag, sonic reflection, ultrasonic transmission, microseismology, resistivity, electrical potential, radar, and thermography. According to this study, radar and thermography were determined to have the greatest potential for development into routine operational procedures because both methods are better suited to rapid assessment of overall conditions of a large number of decks as opposed to defining exact areas (Manning and Holt, 1986).

Benson, et al (1988) conducted a study to make a comparison of methods and equipment to conduct pavement distress surveys. They selected a variety of distress survey procedures employing different levels of automation for field testing. They made the comparative evaluation from several perspectives: (1) reliability, (2) field productivity, (3) usefulness, (4) level of automation, (5) accuracy of the surface distress data, (6) ease of processing, and (7) traffic interferences. (Benson, et al, 1988).

Experimental methods are conducted in the laboratory or with selected field specimens . This method is usually designed to find the best condition for making the pavement assessment. Factors such as equipment geometry, lighting angle, suitable survey time, and others are studied in order to get optimum accuracy from the method.

For example, an experimental and theoretical evaluation of infrared

thermography for surveying the condition of bridge decks was conducted by the Ontario Ministry of Transportation (Masliwec, 1988). This research explored the use of a heat transfer model which describes the temperature gradients in a concrete bridge superstructure by measuring temperatures of different layers on the bridge deck and by using thermocouples spaced at different layers. The study showed that optimum operation times in southern Ontario were 10:00 a.m. to 11:00 a.m. for exposed concrete and 12:00 noon to 1:00 p.m. for asphalt covered bridge decks.

The simulation method utilizes appropriate theory and selected principles to simulate the function of equipment and the conditions under which it is used.

For example, El-Korchi and Wittels (1992) used computer simulation to predict the luminance values of cracks in the Portland Cement Concrete. They developed a mathematical model of a crack, validated the model by comparing simulated with actual luminance values, and showed how to apply the model to automation problems. The authors indicated that the simulation results could be used for making predictions and for designing automated pavement inspection system.

Objective

The overall goal or objective of this research effort was to develop a simulation method for studying infrared thermography and to determine the effect of camera geometry on the ability of the camera system to detect pavement cracks. The goal will be accomplished through the following tasks:

1. Select a simple radiative heat transfer model and identify the

assumptions necessary to model the energy exchanges between elements on a clear pavement sample and on the infrared sensor or camera focal plane.

2. Make modifications to the simple radiation model so that elements on cracked or defective pavements may also be included in the model.
3. Develop the algorithms for creating a digital image using the simple radiative heat transfer model for clear and defective pavements. These algorithms include those necessary to implement the thermal and geometric aspects of the problem.
4. Write a computer program using the algorithms to create a digital image of a section of a simulated, defective pavement. Images will be created for various camera geometry and camera characteristics.
5. Analyze the simulated images for relationships between camera geometry and the ability to identify defects using digital image processing.

Organization of Thesis

This thesis consists of six chapters. Chapter I is an outline of the need for a distress measurement method as part of an automated highway pavement evaluation system. In Chapter II, a review of the theory and application of infrared thermographic image systems is given. In Chapter III, the simulation model needed to create a simulated image is described. Chapter IV is a description of the procedure to implement the simulation model. Chapter V presents the results and an analysis of the data. Chapter VI has a summary of the study, presents the conclusion, and provides recommendations for future research.

CHAPTER II. LITERATURE REVIEW

Principle of Infrared Thermography

Infrared thermography is a non-contact means of producing visible images from the invisible infrared thermal energy emitted from an object. This technique works on the principle that different materials emit different thermal energy. All materials continuously emit and absorb infrared thermal energy by lowering or raising their molecular energy levels (Modest, 1993). The strength of the emission depends on the temperature of the emitting material. As an object becomes hotter, its molecular activity increases and causes that object to generate more energy (Bernard, 1970). Only at absolute zero (-273°C), where all molecular activity stops, will an object cease to emit infrared radiation. Infrared radiation obeys many of the laws that apply to light. When infrared radiation impinges on an object, some of the irradiation will be reflected away from that surface, a fraction will be absorbed inside the layer, and the rest will be transmitted through the surface (Modest, 1993).

Other important factors that describe the thermal characteristics of a material include: 1) emissivity, 2) emissive power, and 3) thermal conductivity. Emissivity is defined as the ratio of energy emitted from a surface to that from a black surface at the same temperature. It is a measure of the ability, or ease, with which an object, or surface, emits infrared radiation. For example, the emissivity of the concrete at 20°C is 0. 92 (Hudson, 1969). Modest (1993) describes the black surface as: "when an electromagnetic wave traveling through a medium strikes the surface of another medium, and any nonreflected part will

penetrate into the medium. While passing through the medium the wave may become continuously attenuated. If attenuation is complete so that no penetrating radiation reemerges, it is known as opaque . . . an opaque surface that does not reflect any radiation is called a perfect absorber or a black surface." The radiative energy emitted from a surface is called emissive power which is a measure of the rate at which radiative heat flux is leaving a surface. The surface, however, can influence the value of the emissive power. Thermal conductivity is a measure of the rate at which heat will pass through a material while thermal capacity is the ability of a material to store heat. For example, concrete pavement has a relatively poor thermal conductivity and capacity as compared to loose sand or water. Therefore, concrete will hold its body temperature relatively longer than cracks containing sand or water. This temperature differential can be detected by a sensitive infrared scanner in real time.

Case Histories

The military developed practical applications of thermal imaging in the 1950s to locate targets and to allow surveillance in darkness. Today, thermal or infrared (IR) imaging is found in other fields of application such as medicine and nondestructive testing and evaluation (Pla and Eberhard, 1990). Infrared thermography has been more fully developed as a commercial technique for detecting delamination in concrete bridge decks (Masliwec, 1988) and (Kunz and Eales, 1985). More recently it has been applied to finding debonding in asphalt-overlaid bridge decks (Maser, et. al., 1990 and Weil, 1992).

The infrared technique was used to help determine where bridge decks were delaminated and where overlays were debonded for two downtown Milwaukee bridges in 1984 (Anonymous, 1985). For this bridge deck study, infrared and video cameras were mounted on a hydraulic mast attached to the front of a remote sensing van and raised approximately 14 feet above the bridge deck. Black-and-white video produced by the IR camera and color video produced by the control camera were displayed on monitors in the van. While scanning, the van moved down the center of each traffic lane at approximately five mph. The van was stopped periodically at an area of suspected delamination or debonding and sounding was used to confirm the infrared data. Results of the IR survey were compiled into data files which allowed the Wisconsin DOT to evaluate rehabilitation alternatives and determine a cost-effective repair.

Research studies were conducted by Manning and Holt (1986) to develop a method for the rapid and automatic collection of data on the condition of bridge decks. As a result of these studies, a system called the deck assessment by radar and thermography (DART) was developed. The system utilizes two basic systems: impulse radar and infrared thermography. A prototype vehicle was equipped with both the radar and thermography equipment. The vehicle is driven slowly across the bridge deck and the data are collected and stored on a magnetic tape. Studies showed: 1) a delamination in the concrete deck slab produced a temperature difference during periods of heating, 2) the maximum difference in surface temperature recorded at the bridge deck was 2°C at 2 p.m., and 3) optimum operation times were limited to 11 a.m. to 2 p.m. The ability

to detect delaminations on asphalt-covered decks was also found to be much more sensitive to atmospheric conditions such as wind, humidity, and cloud cover than on exposed concrete decks. The DART infrared system only provides a two-dimensional surface image of a bridge deck, but when combined with the radar system of DART, three-dimensional images may be obtained.

EnTech Engineering Inc. (Weil, 1992) has performed bridge deck inspections with the use of infrared thermography and ground penetrating radar for the Illinois Department of Transportation. This program proved to be very successful. During a first pass over any pavement, only the infrared thermography data were collected and then presented on a scaled drawing. Then a second pass on the pavement was made using only the ground penetrating radar system. The radar antenna was placed only on the specific anomalies located on the drawings. Once the anomaly location designated on the drawing was confirmed by the radar information, then each anomaly was characterized as to whether it was caused by a debonding of the overlay, a void, or delamination above or below the rebar. Multiple year repeat inspections on many of the deck pavements have confirmed the repeatability of the method and have eliminated the need for physical coring and major traffic control during inspection (Weil, 1992).

The infrared thermographic technique was used to inspect a two-lane section of Interstate 70, approximately 4,000 feet in length in 1991 (Weil, 1992). The reason for the inspection was due to the entire area being rehabilitated with all new concrete slabs as a result of massive deterioration. After the new slabs

had been poured, Missouri DOT officials felt that the concrete mixture used may not have been completely homogeneous and that pockets of pure sand, with no binder or gravel, may have found their way into the pavement. After the inspection, five anomaly areas were located. A check of the five areas found that four contained loose sand or voids, while the fifth area apparently had excess concrete and miscellaneous debris that had not been removed during the initial tear-out of the old pavement.

In 1990, the pavement of the New Hampshire International Airport was completely inspected using infrared thermographic techniques. The inspection took three nights and was performed without the interruption of air traffic. The inspection was made because the landing gear of a DC-10 carrying a full load of passengers fell into a void under the taxiway pavement. The void was 6 ft. by 6 ft. by 8 ft. in size. The inspection uncovered subsurface voids of varying sizes. Several of the voids could have caused major damage to airplanes if the pavement above them had collapsed (Weil, 1992).

Advantages and Disadvantages

The advantages of using infrared thermography for pavement evaluation include: minor interruptions of traffic flow and labor and time savings. The technique does not require the high-powered supplemental lighting required by a conventional camera system such as the PASCO ROADRECON SYSTEM (Benson, 1988). Weil (1989) stated that it is also intrinsically safe, emitting no radiation, when compared to other methods such as electrical or magnetic

methods, acoustic emission, and ground probing radar.

The disadvantages of this technique include sensitivity to pavement conditions and weather conditions. Several previous studies have indicated these drawbacks. For instance, Masliwec (1988) showed that infrared thermography cannot be used if any form of moisture is present on the bridge deck. Furthermore, he explained if water has accumulated in a delaminated area, it will act as a continuum for the impinging solar radiation. Since water has a large latent heat of vaporization, most of the surface heat will be absorbed and transferred by the water. As a result, a delamination will not be detected by the infrared system. Manning and Holt (1986) indicated that the oil spots and debris on the deck make the recognition of the delamination difficult in the infrared image. Dean and Kadir (1992) showed that the duration of sun exposure and cloud cover affect the quality of the infrared image. Their interpretation was that the presence of cloud cover blocks radiation from the sun and may cause the surface temperature of the cracks to reduce faster than the sound pavement. As a result, the temperature differential between the cracks and sound pavement was reduced, producing a poor image for digital image processing. They also indicated that weather conditions such as air temperature, relative humidity, and wind speed could affect the results. Other disadvantages are that the infrared image does not give information on the depth of the flaws, but only the plane location and dimensions. Furthermore, the interpretation of the output image is not simple.

Image processing system

An overview of an image processing system will reflect the ERDAS

image processing system (ERDAS Inc., 1991). As a result, some of its contents or conventions might be different from other image processing systems.

There are two types of image data files used in ERDAS: LAN and GIS files. LAN files are typically generated by remote sensing, aerial sensors, or video cameras. LAN data file values represent a quantity such as a measurement of light, emitted heat, and others. GIS files are usually created by classifying or rescaling LAN files. The information contained in a GIS file typically represents a category or type such as sound pavement and defective pavement. ERDAS data sets are structured to produce images from digitized data. Data sets are made of up of groups of pixels organized in a two-dimensional coordinate system in a grid pattern along an X and Y axis. A pixel or picture element, is the smallest part of a picture which can be visualized as a single point of light on a video display screen. Each pixel has a specific data or brightness value, and its location is expressed as a pair of X and Y coordinates. The brightness of each pixel has a numerical value ranging from zero for black to some higher number for white. An 8-bit series is commonly used to represent the gray-scale value with 0 for black and 255 for white. Image data are stored in a data file on a computer disk or optical media. The data consist only of numbers. ERDAS system includes three main functions: image rectification, image enhancement, and image classification. In this research, the ERDAS system was used to process LAN and GIS image data which were created by the simulation method.

CHAPTER III. COMPONENTS OF THE SIMULATION MODEL

Thermal Components

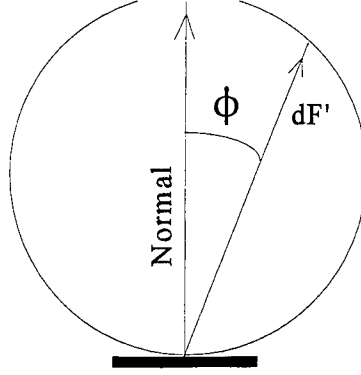
General radiation heat transfer model

Radiation is one of the three mechanisms of heat transfer: conduction, convection, and radiation. Radiation is the transmission of energy by electromagnetic waves; the energy transmitted is called radiant energy. All bodies at a temperature above absolute zero emit infrared radiation that corresponds to the portion of the electromagnetic spectrum $1\mu\text{m} - 1000\mu\text{m}$ (Modest, 1993). Infrared radiation is subject to certain general laws.

One of the fundamental laws of the radiation theory is Lambert's law (Bramson, 1968) which expresses the variation of the directional radiant flux (F') (watts/sr) with the angle (ϕ) of observation. Radiant flux refers to a rate of transfer of radiant energy. Directional radiant flux refers to a ratio of radiant flux to the value of a solid angle in a given direction. Directional radiant flux is also called Radiant intensity (watts/sr). Another related concept is radiance (I) (watts/cm²/sr) which refers to a ratio of radiant intensity to area of radiating surface as projected on plane normal to a given direction. Lambert's law is applicable to a blackbody and to a perfectly scattering or diffuse surface. Such a surface has the same radiance in all directions, and the directional radiant flux (F') of a surface element will vary in proportional to the cosine of the angle (ϕ) between the normal to the surface and the given direction. The mathematical formulation of Lambert's law is:

$$dF' = I \cdot dS' \cdot \cos(\phi') \quad (\text{watts/sr}) \quad \text{Equation 1.1}$$

The law may be represented graphically in the plane as a circle tangent to the radiating surface at the given point, and in space as a spherical surface, obtained by rotating the circle about the normal (Figure 3).



ϕ = angle between the normal to the surface and
the given direction

dF' = directional emitted flux

Figure 3. Graphical interpretation of Lambert's law.

With Lambert's law, the energy exchange between two elements dS and dS' can be analyzed, and quantified as:

$$dQ = I \cdot dS \cdot \cos(\phi) \cdot d(\omega) \quad (\text{watts}) \quad \text{Equation 1.2}$$

consider a solid angle:

$$d(\omega) = dS' \cdot \cos(\phi') / r^2 \quad (\text{sr}) \quad \text{Equation 1.3}$$

whence:

$$dQ = I \cdot dS \cdot dS' \cdot \cos(\phi) \cdot \cos(\phi') / r^2 \quad (\text{watts}) \quad \text{Equation 1.4}$$

where two elements dS and dS' are separated by distance r , having normals \mathbf{n} and \mathbf{n}' with the angle (ϕ) and (ϕ') , respectively (Figure. 4). Equation 1.1 is the basic model that is used in the simulation procedure of this research.

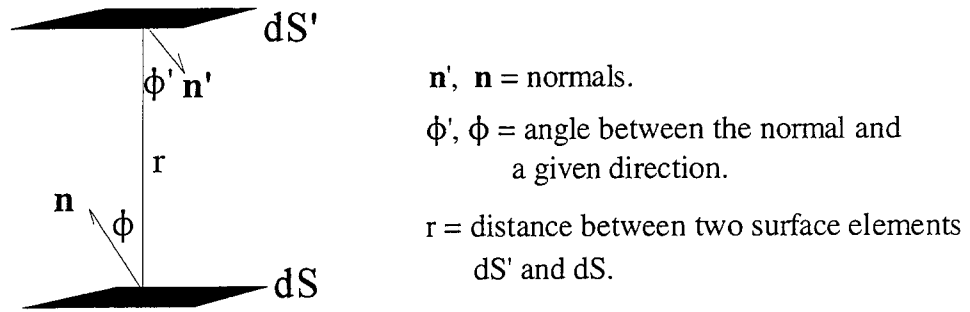


Figure 4. Energy exchange between two surface elements.

The radiative intensity (I) leaving a diffuse surface (or any surface whose outgoing intensity is independent of direction) may be evaluated from the surface emissive power (E) as:

$$I = E / \pi \quad (\text{watts/cm}^2/\text{sr}) \quad \text{Equation 2}$$

The relationship has been derived in (Bramson, 1968 and Modest, 1993). The (E) is total emissive power which corresponds to all electromagnetic wavelengths. Based on the Stefan-Boltzmann law, the emissivity power is generally proportional to the temperature to the fourth power, i. e. :

$$E = \epsilon \cdot \sigma \cdot T^4 \quad (\text{watts/cm}^2) \quad \text{Equation 3}$$

where:

ϵ = material emissivity (watts/watts)

σ = boltzmann constant (watts/cm²/K⁴)

T = temperature (in degrees Kelvin)

By substituting Equation (2) and (3), Equation (1.4) can be expressed as:

$$dQ = (E/\pi) \cdot dS \cdot dS' \cdot \cos(\phi) \cdot \cos(\phi') / r^2 \text{ (watts)}$$

or:

$$dQ = (\epsilon \sigma T^4) / \pi \cdot dS \cdot dS' \cdot \cos(\phi) \cdot \cos(\phi') / r^2 \text{ (watts)} \quad \text{Equation 4}$$

And substituting finite differences for differential elements, the Equation (4) can be converted to:

$$\Delta Q = (E) / \pi \cdot \Delta S \cdot \Delta S' \cdot \cos(\phi) \cdot \cos(\phi') / r^2 \text{ (watts)}$$

or:

$$\Delta Q = (\epsilon \sigma T^4) / \pi \cdot \Delta S \cdot \Delta S' \cdot \cos(\phi) \cdot \cos(\phi') / r^2 \text{ (watts)} \quad \text{Equation 5}$$

Equation (5) is the expression used for calculating the radiative heat energy emitted from a pavement surface.

The assumption of applying Lambert's law is that the radiative surface is a diffuse (or matter) one. In this research, the simulation surface is a concrete pavement surface. So it is assumed that the concrete material surface is a diffuse surface. The researchers' Norman Wattles and Thor El-korch (1992) have validated this assumption in their study.

Determination of the infrared fraction of the emissive power (E). A thermal infrared camera can sense the radiation within the electromagnetic band which is the portion of the electromagnetic spectrum corresponding to the heat radiation. However, the emissive power (E) is the total emissive power corresponding to all of the electromagnetic spectrum. Therefore, the fraction of emissive power which falls in the infrared thermal electromagnetic band must be determined. Modest (1993) has given the equation to calculate it (Equation 6).

$$\int_0^\lambda E_\lambda d\lambda = [f(n\lambda_2 T) - f(n\lambda_1 T)] n^2 \sigma T^4 \quad \text{Equation 6}$$

where:

λ = wavelength.

E_λ = emissive power of λ .

T = temperature.

σ = boltzmann constant.

n = index of refraction.

Equation (6) is a function in a single variable $n\lambda T$ and is tabulated in the Appendix. For example, to find the fraction of total emission falling into the infrared spectrum band ($\lambda_1 = 8\mu\text{m}$ and $\lambda_2 = 14 \mu\text{m}$) with the temperature $T = 20^\circ\text{C} = 293^\circ\text{K}$, and the n approximately equals to one, then:

$$n\lambda_1 T = 1 \cdot 14 \cdot 293 = 4102 \mu\text{mk}$$

$$n\lambda_2 T = 1 \cdot 8 \cdot 293 = 2344 \mu\text{mk}$$

From the Appendix,

$$F(n\lambda_2 T) = 0.4982$$

$$F(n\lambda_1 T) = 0.1300$$

$$F(n\lambda_2 T) - F(n\lambda_1 T) = 0.3682$$

Therefore with a bandwidth of $6\mu\text{m}$ ($14\mu\text{m}-8\mu\text{m}$), the energy emitted is 37% of the total emitted energy.

It is assumed that the infrared energy emitted from a concrete pavement surface has the same relationship to the total energy emitted as did the black body in the previous discussion. If this assumption is in error, it does not affect the results of the simulated image processing since the image is a gray level

which is converted from the value of radiative energy by a linear relationship.

It can be proven as follows:

Let:

$$B_i = \text{gray level pixel value} \quad (i = 1, 2, \dots, n)$$

$$b_{ma} = \max \{ B_i \}$$

$$b_{mi} = \min \{ B_i \}$$

$$Q_i = \text{energy from infrared} \quad (i = 1, 2, \dots, n)$$

$$q_{ma} = \max \{ Q_i \}$$

$$q_{mi} = \min \{ Q_i \}$$

$$Q'_i = \text{total energy} \quad (i = 1, 2, \dots, n)$$

$$q'_{ma} = \max \{ Q'_i \}$$

$$q'_{mi} = \min \{ Q'_i \}$$

With the linear relationship between Q and B, as follows:

$$\frac{Q - q_{mi}}{q_{ma} - q_{mi}} = \frac{B - b_{mi}}{b_{ma} - b_{mi}} \quad \text{Equation 7}$$

For any wavelength band $\Delta\lambda$:

$$Q = x \cdot Q'$$

where: x = ratio of total energy and the energy from $\Delta\lambda$

then:

$$q_{mi} = \min \{ Q_i \} = \min \{ x \cdot Q' \} = x \cdot \min \{ Q' \} = x \cdot q'_{mi}$$

$$q_{ma} = \max \{ Q_i \} = \max \{ x \cdot Q' \} = x \cdot \max \{ Q' \} = x \cdot q'_{ma}$$

so the linear Equation (7) becomes:

$$\frac{Q - q_{mi}}{q_{ma} - q_{mi}} = \frac{x \cdot Q' - x \cdot q'_{mi}}{x \cdot q'_{ma} - x \cdot q'_{mi}} = \frac{Q' - q'_{mi}}{q'_{ma} - q'_{mi}} = \frac{B - b_{mi}}{b_{ma} - b_{mi}} \quad \text{Equation 8}$$

Equation (8) indicates that with the linear relationship, the infrared energy has the same gray level as that of the total energy. Therefore, the gray level converted from either the energy from the infrared portion or the total energy will be the same. Also, an error in calculating the infrared portion of the total energy will have no effect on the gray level.

Modeling of defective pavement with V-shaped cracks

The emissive power (E). When the pavement has a defect-free or sound surface, the emissive power of it can be determined by the Stephen-Boltzmann law, as defined by Equation 3. However, when the pavement has cracks on the surface, the emissive power will be more complicated because the radiative heat flow on the crack sidewalls will interact. The assumption for this research is that the crack is V-shaped in cross section. This is because most often cracks are V-shaped beginning at the surface of the pavement (Anonymous, 1992). The governing equation for computing the emissive power of a V-shaped crack is expressed by (Sparrow, et al, 1961) as follows:

$$E(x) = \epsilon \sigma T^4 + 0.5(\rho(1 - \cos^2\beta) \int_0^L E(y) \frac{xy}{(x^2 + y^2 - 2xy\cos\beta)^{3/2}} dy) \quad (\text{watts/cm}^2)$$

Equation 9

where:

$E(x)$ = emissive power on x side (refer to Figure 5).

$E(y)$ = emissive power on y side (refer to Figure 5).

$\rho = 1 - \epsilon$.

β = vertex angle (refer to Figure 5).

ϵ = material emissivity. (watts/watts)

σ = boltzmann constant. (watts/cm²/K⁴)

T = temperature. (in degrees Kelvin)

$E(x)$ and $E(y)$ have the same characteristic. They are the variables to be solved in Equation 9. The profile of a V-shaped crack is shown in Figure 5. Because of the geometric and thermal symmetry (same radiation properties), the distribution of the emissive power (E) will be the same along both sidewalls.

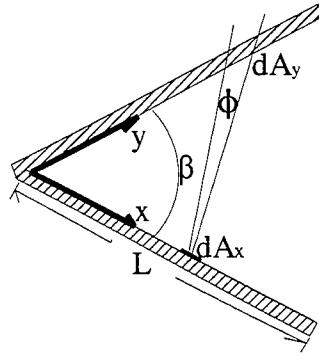


Figure 5. V-shaped crack.

Solution to emissive power calculation. Equation (9) is called an integral equation, since the unknown variable (E) appears under the integral sign as well as in other parts of the equation. Equation (6) may be expressed as a dimensionless form:

$$E(X) = 1 + 0.5 \times \rho(1 - \cos^2 \beta) \int_0^1 E(Y) \frac{XY}{(X^2 + Y^2 - 2XY \cos \beta)^{3/2}} dY$$

where

$$\rho = 1 - \varepsilon$$

$$E(X) = \frac{E(x)}{\varepsilon \sigma T^4}, \quad E(Y) = \frac{E(y)}{\varepsilon \sigma T^4}$$

Equation 10

The integral Equations (9) or (10) can be solved by using a numerical method. Equation (10) is solved numerically as follows:

Let:

$$h = 1/n \quad (n \text{ is an integer})$$

$$G = 0.5 \rho (1 - \cos^2 \beta)$$

then:

$$E(Y_1) = 1 + G \times \sum_1^n E(Y_i) \frac{Y_1 Y_i h}{(Y_1^2 + Y_i^2 - 2Y_1 Y_i \cos \beta)^{3/2}}$$

$$E(Y_2) = 1 + G \times \sum_1^n E(Y_i) \frac{Y_2 Y_i h}{(Y_2^2 + Y_i^2 - 2Y_2 Y_i \cos \beta)^{3/2}}$$

.....

$$E(Y_n) = 1 + G \times \sum_1^n E(Y_n) \frac{Y_n Y_i h}{(Y_n^2 + Y_i^2 - 2Y_n Y_i \cos \beta)^{3/2}}$$

where

$$Y_i = i \times h \quad (i = 1, 2, \dots, n)$$

re-organize the equations above:

$$-1 = G \times \sum_1^n E(Y_i) \frac{Y_1 Y_i h}{(Y_1^2 + Y_i^2 - 2Y_1 Y_i \cos \beta)^{3/2}} - E(Y_1)$$

$$-1 = G \times \sum_1^n E(Y_i) \frac{Y_2 Y_i h}{(Y_2^2 + Y_i^2 - 2Y_2 Y_i \cos \beta)^{3/2}} - E(Y_2)$$

.....

$$-1 = G \times \sum_1^n E(Y_n) \frac{Y_n Y_i h}{(Y_n^2 + Y_i^2 - 2Y_n Y_i \cos \beta)^{3/2}} - E(Y_n)$$

or , write the equations above as an array form:

let:

$$F(Y_j, Y_i) = \frac{Y_j Y_i}{(Y_j^2 + Y_i^2 - 2Y_j Y_i \cos \beta)^{3/2}} \quad (j, i = 1, 2, \dots)$$

$$F_{n \times n} = \begin{bmatrix} F(Y_1, Y_1) - 1 & F(Y_1, Y_2) & \dots & F(Y_1, Y_n) \\ F(Y_2, Y_1) & F(Y_2, Y_2) - 1 & \dots & F(Y_2, Y_n) \\ \dots & \dots & \dots & \dots \\ F(Y_n, Y_1) & F(Y_n, Y_2) & \dots & F(Y_n, Y_n) - 1 \end{bmatrix}$$

$$E_{n \times 1} = \begin{bmatrix} E(Y_1) \\ E(Y_2) \\ \dots \\ E(Y_n) \end{bmatrix} \quad I_{n \times 1} = \begin{bmatrix} 1 \\ 1 \\ \dots \\ 1 \end{bmatrix}$$

then:

$$(G \times h) \times F_{n \times n} \times E_{n \times 1} = -I_{n \times 1}$$

Equation 11

Given a vertex angle β and the material emissivity ϵ , the emissive power (E) can be obtained by solving Equation (11). For example, the Figures 6, 7, and 8 are the emissive power (E) values corresponding to the emissivity $\epsilon = 0.92$, and the vertex angles 60° , 45° and 30° respectively. For example, emissive power of a V-shaped crack with 60° vertex angle is about 1.03 times emissive power of the sound surface.

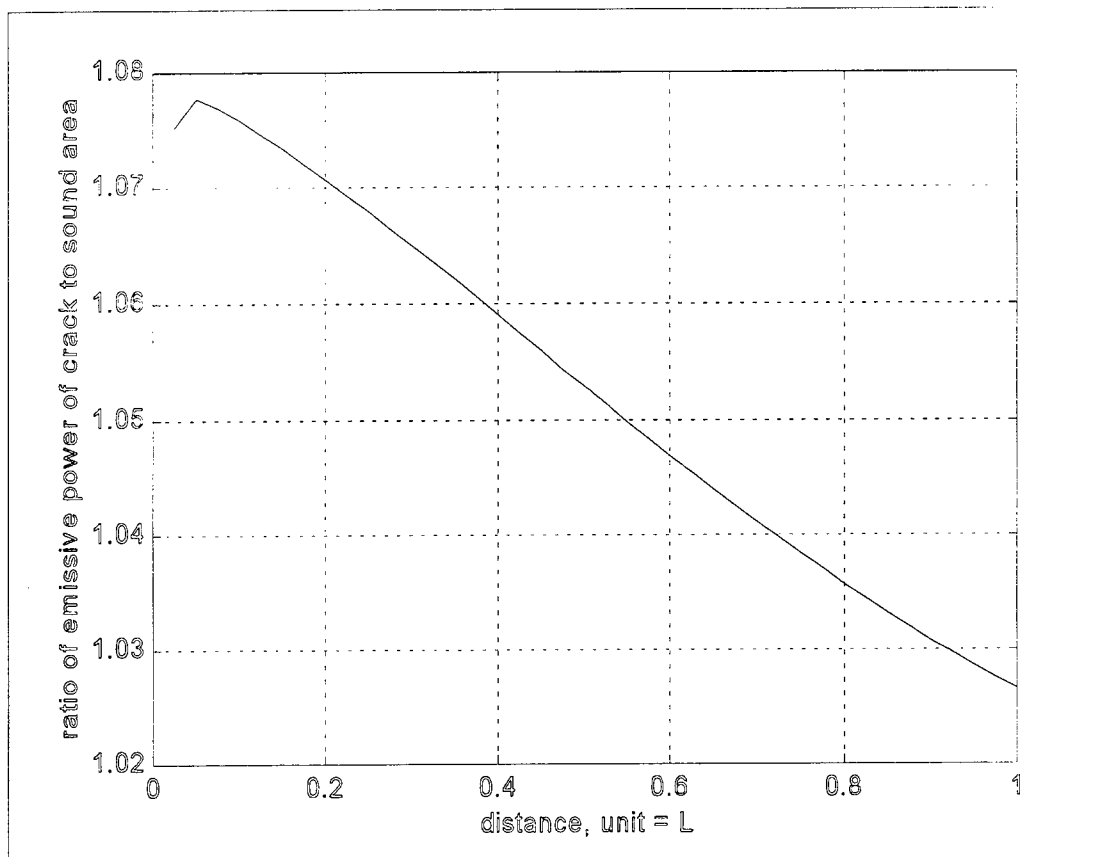


Figure 6. Emissive power of a V-shaped crack with a vertex angle of 60° .

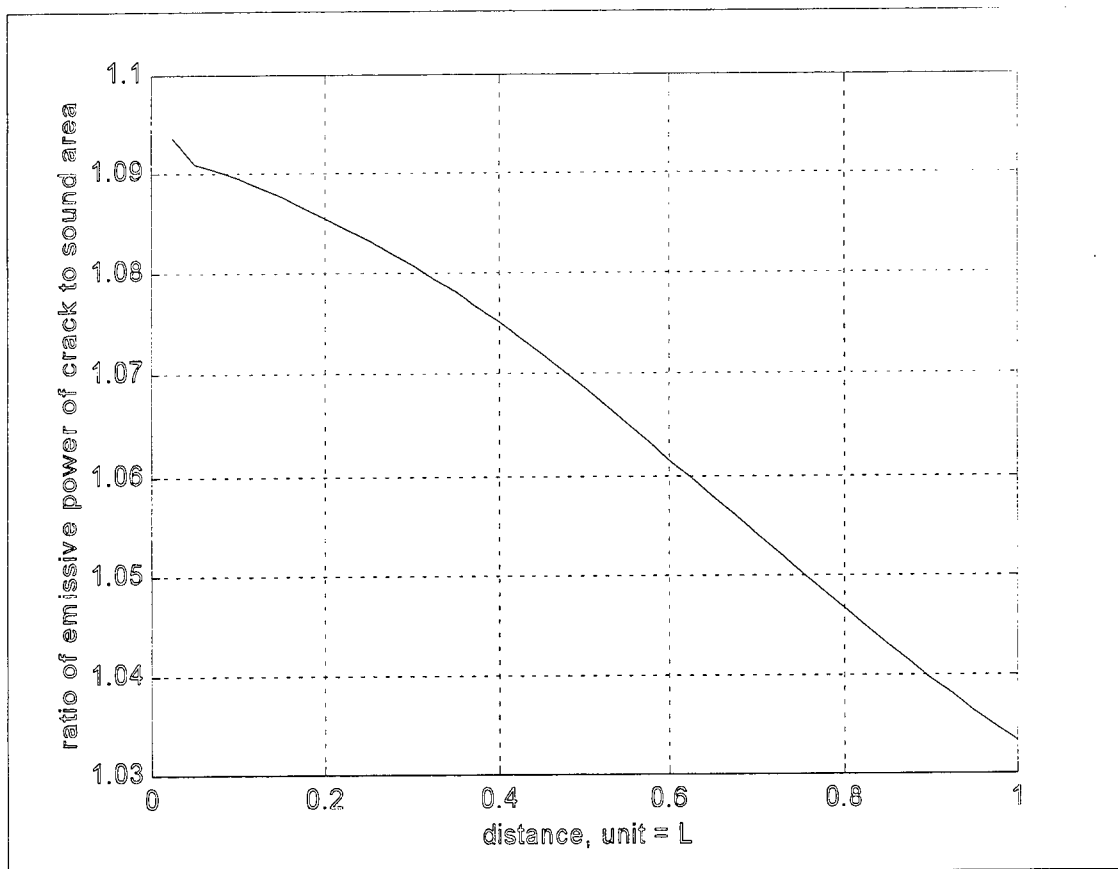


Figure 7. Emissive power of a V-shaped crack with a vertex angle of 45° .

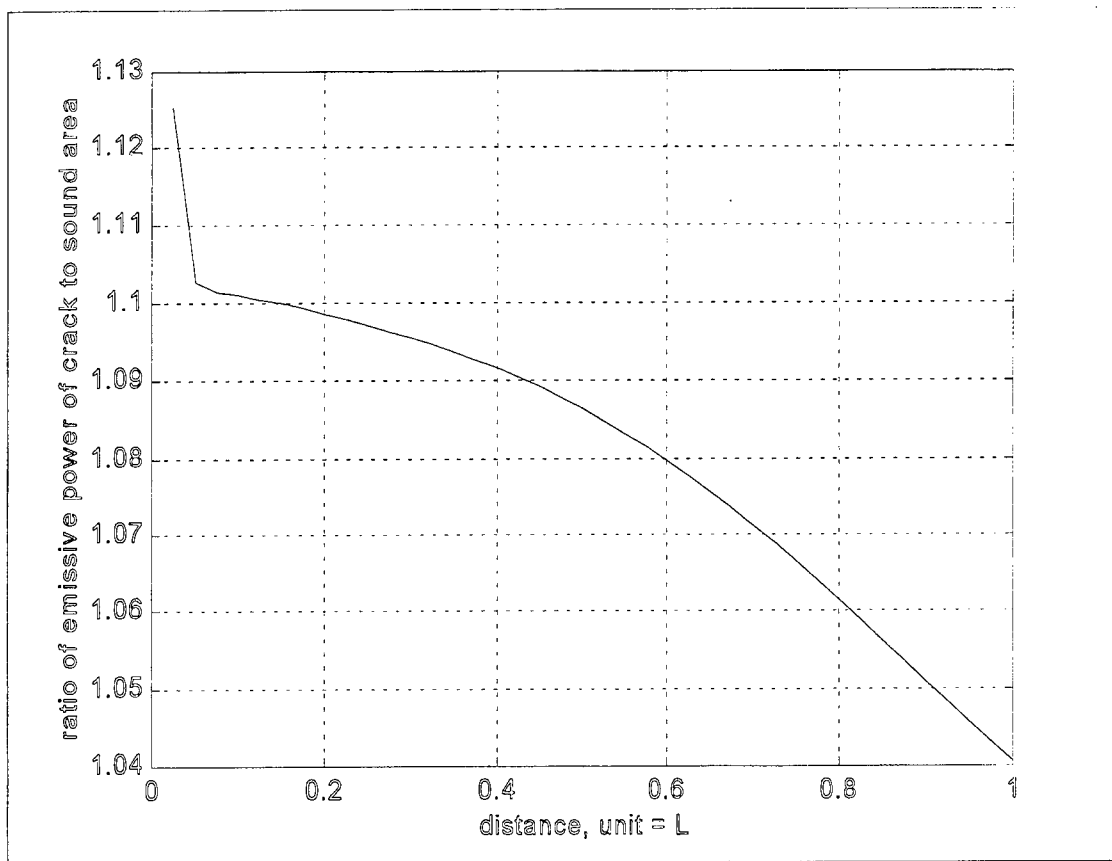


Figure 8. Emissive power of a V-shaped crack with a vertex angle of 30° .

Camera Component

All infrared systems require a transmitter and a receiver. Optics may be used at the transmitter to shape, direct, or modify the infrared radiation before it reaches the receiver. The receiver may use optical techniques to help collect and focus the incoming radiation onto an infrared detector. The heat transfer model above describes the energy exchange between the emitting area and the receiving area. To model an infrared imaging system, the image frame size and pixel size must be known. Infrared cameras have a 1-inch tube. The size of the scanned area in the tube is 12.8 mm (width) and 9.6 mm (height) (McGinty, 1988). There are 512 lines scanned at every image frame in the scanned area, and about 480 lines are effective. So the width of each scanned line is about 0.02 mm ($9.6/480$) which represents the pixel size and the size of the scanned area measured in pixels is, 640 pixels ($12.8/0.02$) by 480 pixels ($9.6/0.02$). The shapes of the sample areas selected in this research, however, are square and the shapes projected on the sensor plane are square too when the tilt angle is zero. A sensor plane of 542 by 482 pixels was chosen for the simulated camera. This dimension provides for a measure of error tolerance and maintains a rectangular-shaped sensor plane.

A two-dimension, right-handed Cartesian coordinate system (x, y) is assigned to the infrared camera sensor plane as shown in Figure 9. The rectangle represents the image frame and the simulated images from different camera geometries will be formed on it. The unit of this coordinate system is a pixel number.

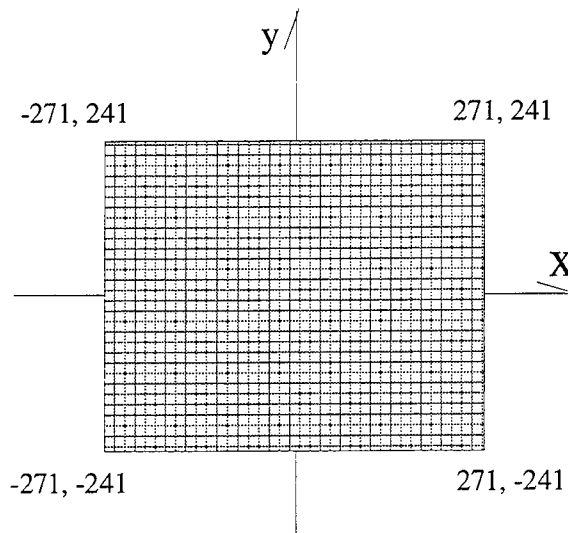


Figure 9. Coordinate system on the sensor plane.

Geometric Component of the Model

As can be seen in Equation 5, there are two characteristic parts to it: one is the thermal part (E) and the other is the geometric part. The thermal part (E) can be determined based on the theory presented in the section on **Thermal components**. The geometry component will be determined in this section.

Coordinate system

The infrared camera, consists of two basic components, the lens and the sensor plane. An analog image, that is formed when the radiative energy passes through the camera lens and onto the sensor plane, is composed of a rectangular grid of intensity values. Each element of this rectangular grid is referred to as a picture element or pixel. When the camera scans the pavement at a vertical position, the sensor plane is parallel to the pavement surface. When the camera

is at a tilt angle position, the sensor plane is not parallel to the surface (shown in Figure 10).

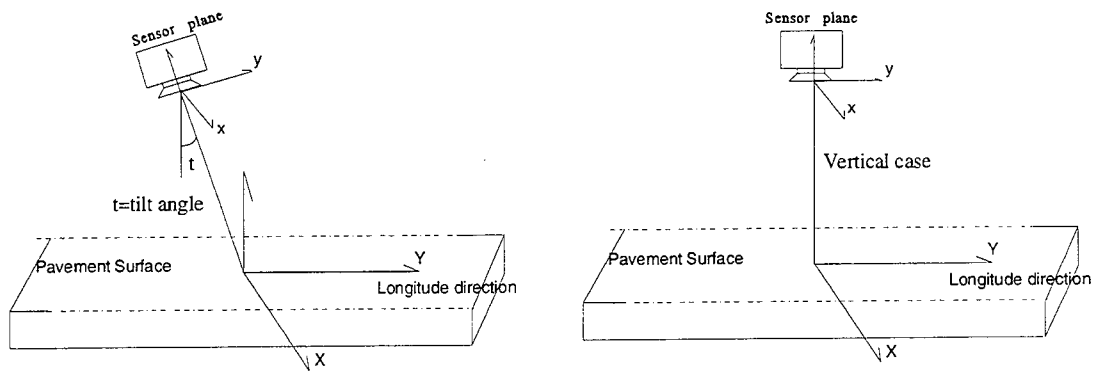


Figure 10. The camera scanning a pavement section.

To calculate the geometric variables (angle or cosine value, finite areas and length (r)) on two different planes (sensor plane and the surface), it is convenient to establish two coordinates system on the two planes, a coordinate system of the sensor plane named the image space system x, y, z and a coordinate system of the pavement surface named the object space system X, Y, Z . These two coordinate systems are shown in Figure 11.

$$\begin{bmatrix} x \\ y \\ z \end{bmatrix} = \mathbf{M} \begin{bmatrix} X \\ Y \\ Z \end{bmatrix} \quad \text{or} \quad \mathbf{v} = \mathbf{M}\mathbf{V} \quad \text{Equation 12}$$

in which \mathbf{v} is the vector in the x, y, z system and \mathbf{V} is the vector in the X, Y, Z system.

Since the orientation matrix \mathbf{M} is orthogonal, its transpose \mathbf{M}^T is equal to its inverse \mathbf{M}^{-1} . Then

$$\mathbf{V} = \mathbf{M}^T \mathbf{v} \quad \text{or} \quad \begin{bmatrix} X \\ Y \\ Z \end{bmatrix} = \mathbf{M}^T \begin{bmatrix} x \\ y \\ z \end{bmatrix} \quad \text{Equation 13}$$

The nine elements of \mathbf{M} are the cosines of the spatial angles that each of the axes x, y, z makes with each of the axes X, Y, Z . That is:

$$M = \begin{bmatrix} \cos(xX) & \cos(xY) & \cos(xZ) \\ \cos(yX) & \cos(yY) & \cos(yZ) \\ \cos(zX) & \cos(zY) & \cos(zZ) \end{bmatrix} = \begin{bmatrix} m_{11} & m_{12} & m_{13} \\ m_{21} & m_{22} & m_{23} \\ m_{31} & m_{32} & m_{33} \end{bmatrix} \quad \text{Equation 14}$$

Collinearity equations

The geometry of a camera is based on the principle of perspective or central projection. Referring back to Figure 11, at the instant of sensing the image, the image vector **a** from the exposure station (L) (lens' center) to the image point a and the object vector **A** from L to the object point A are collinear. Two vectors (**a** and **A**) are said to be collinear if one is a scalar multiple of the other. Thus:

$$\mathbf{a} = k \mathbf{A} \quad \text{Equation 15}$$

in which (k) is a scalar that is equal to the ratio of the length of **a** to the length **A**. Equation (12) may be expressed in the form of the components of the two vectors(**a** and **A**) provided that both vectors are referred to the same coordinate system. From Figure 12, vector **a** is directed from L to a, the components of **a** in the x, y, z system are:

$$\mathbf{a} = \begin{bmatrix} x_a \\ y_a \\ -f \end{bmatrix} \quad \text{Equation 16}$$

and from Figure 11, the components of \mathbf{A} in the X, Y, Z system are:

$$\mathbf{A} = \begin{bmatrix} X_A - X_L \\ Y_A - Y_L \\ Z_A - Z_L \end{bmatrix} \quad \text{Equation 17}$$

In order to express the components \mathbf{A} in the x, y, z system, it must be pre-multiplied by \mathbf{M} according to Equation (12) and then Equation (15) because

$$\mathbf{a} = k\mathbf{M}\mathbf{A} \quad \text{Equation 18}$$

or:

$$\begin{bmatrix} x_a \\ y_a \\ -f \end{bmatrix} = k \cdot \mathbf{M} \begin{bmatrix} X_A - X_L \\ Y_A - Y_L \\ Z_A - Z_L \end{bmatrix} \quad \text{Equation 19}$$

Since the \mathbf{M} is an orthogonal matrix, so:

$$\mathbf{A} = (1/k) \bullet \mathbf{M}^T \bullet \mathbf{a} \quad \text{Equation 20}$$

and:

$$\begin{bmatrix} X_A - X_L \\ Y_A - Y_L \\ Z_A - Z_L \end{bmatrix} = (1/k) \bullet \mathbf{M}^T \begin{bmatrix} x_a \\ y_a \\ -f \end{bmatrix} \quad \text{Equation 21}$$

Equations (19) through (21) are different forms of the collinearity equations. They express the fundamental relationship that the perspective center, the image point, and the object point lie on a straight line (or say a single image ray). Any individual ray in the frame image bundle is expressed by the collinearity equations. The nine elements of the orientation matrix are constant for all rays in the bundle. Since the image of an object is a two-dimensional representation of a generally three-dimensional object, the scale is different from one image point to another. Consequently the scaler (k) in Equations (18) through (21) takes on a different value for each ray in the bundle. Since (k) is usually unknown, it is eliminated from consideration as follows. Expanding Equation (19) by substituting the right side of Equation (14) for \mathbf{M} , and dropping subscripts a and A gives:

$$\begin{bmatrix} x \\ y \\ -f \end{bmatrix} = k \begin{bmatrix} m_{11} & m_{12} & m_{13} \\ m_{21} & m_{22} & m_{23} \\ m_{31} & m_{32} & m_{33} \end{bmatrix} \begin{bmatrix} X - X_L \\ Y - Y_L \\ Z - Z_L \end{bmatrix} \quad \text{Equation 22}$$

Multiplying through the right side and equating to the terms of the left side gives:

$$x = k[m_{11}(X - X_L) + m_{12}(Y - Y_L) + m_{13}(Z - Z_L)] \quad \text{Equation 23.1}$$

$$y = k[m_{21}(X - X_L) + m_{22}(Y - Y_L) + m_{23}(Z - Z_L)] \quad \text{Equation 23.2}$$

$$-f = k[m_{31}(X - X_L) + m_{32}(Y - Y_L) + m_{33}(Z - Z_L)] \quad \text{Equation 23.3}$$

Dividing Equations (23.1) and (23.2) by (23.3) gives:

$$x = -f \frac{m_{11}(X - X_L) + m_{12}(Y - Y_L) + m_{13}(Z - Z_L)}{m_{31}(X - X_L) + m_{32}(Y - Y_L) + m_{33}(Z - Z_L)} \quad \text{Equation 24}$$

$$y = -f \frac{m_{21}(X - X_L) + m_{22}(Y - Y_L) + m_{23}(Z - Z_L)}{m_{31}(X - X_L) + m_{32}(Y - Y_L) + m_{33}(Z - Z_L)}$$

The inverse of Equations (24) can be derived from Equations (21) to give

$$X - X_L = (Z - Z_L) \frac{m_{11}(x) + m_{21}(y) + m_{31}(-f)}{m_{13}(x) + m_{23}(y) + m_{33}(-f)}$$

Equation 25

$$Y - Y_L = (Z - Z_L) \frac{m_{12}(x) + m_{22}(y) + m_{32}(-f)}{m_{13}(x) + m_{23}(y) + m_{33}(-f)}$$

In this study, suppose the infrared detector can tilt only along the Y direction of the X, Y, Z object space, which is in the longitudinal direction of the pavement surface (see Figure 11). Thus, the nine elements of orientation in Equation 14 are:

$$\begin{aligned} m_{11} &= \cos (xX) = \cos 0^\circ = 1 & m_{12} &= \cos (xY) = \cos 90^\circ = 0 \\ m_{13} &= \cos (xZ) = \cos 90^\circ = 0 \\ m_{21} &= \cos (yX) = \cos 90^\circ = 1 & m_{22} &= \cos (yY) = \cos (t) \\ m_{23} &= \cos (yZ) = \cos (90^\circ - t) = \sin (t) \\ m_{31} &= \cos (zX) = \cos 90^\circ = 0 & m_{32} &= \cos (zY) = \cos (90^\circ + t) = -\sin (t) \\ m_{33} &= \cos (zZ) = \cos (t) \end{aligned}$$

and $(X_L, Y_L, Z_L) = (0, -H \cdot \tan(t), H)$, where H is camera height.

Then Equations (24) and (25) can be reduced as follows (Equations 26, 27):

$$x = -f \frac{X}{-\sin(t) \cdot (Y + H \cdot \tan(t)) + \cos(t) \cdot (Z - H)}$$

Equation 26

$$y = -f \frac{(Y - H \cdot \tan(t)) + \sin(t) \cdot (Z - H)}{-\sin(t) \cdot (Y + H \cdot \tan(t)) + \cos(t) \cdot (Z - H)}$$

$$X = (Z-H) \frac{x}{\sin(t) \cdot (y) + \cos(t) \cdot (-f)}$$

Equation 27

$$Y+H \cdot \tan(t) = (Z-H) \frac{\cos(t) - \sin(t) \cdot (-f)}{\sin(t) \cdot (y) + \cos(t) \cdot (-f)}$$

With the collinearity equations and the image space coordinate of the pixels given, the geometric variables in the simulation model now can be determined.

Finite area ($\Delta S'$ and ΔS)

The radiative heat energy can be received by the sensor plane through the lens' aperture of the detector. In other words, the lens' aperture receives the energy and then focuses it on pixels on the sensor plane. Each pixel views a corresponding small area on the pavement surface. If the small area is called the object, then the corresponding pixel is its image. They have a projective relationship. This projective relationship is referenced to as a perspective or central projection.

Let the lens' aperture be represented by $\Delta S'$ and the small area on pavement by a ΔS . The $\Delta S'$, in this simulation case, is the aperture of an infrared camera INSIGHT 80. The ΔS can be determined with the collinearity Equations. The shape of ΔS is a trapezoid when the detector tilts along the Y-direction only. In this case, the line which is parallel to the x-axis is also parallel to the X-axis after projection and the line which is parallel to the y-axis is not parallel to the Y-axis after projection (shown in Figure 12).

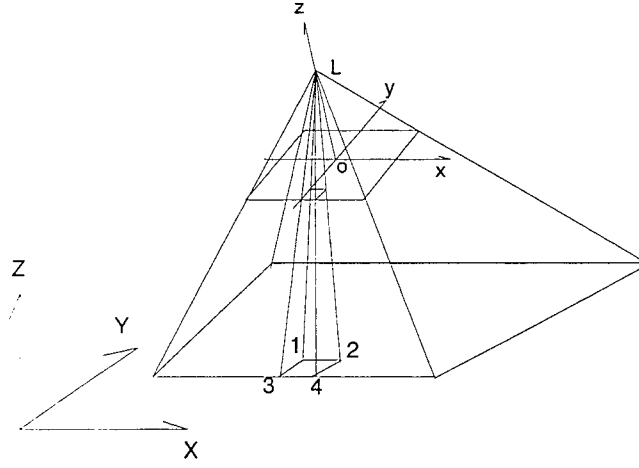


Figure 12. Relationship between pixel and its projected area.

So the area of ΔS is

$$\Delta S = 0.5 \cdot (\Delta X_{1,2} + \Delta X_{3,4}) \cdot \Delta Y_{2,4} \quad (\text{trapezoid area}) \quad \text{Equation 28.1}$$

It is also right in the vertical case since $\Delta X_{1,2} = \Delta X_{3,4}$.

$$\Delta S = 0.5 \cdot (\Delta X_{1,2} + \Delta X_{3,4}) \cdot \Delta Y_{2,4} = 0.5 \cdot (2 \cdot \Delta X_{1,2}) \cdot \Delta Y_{2,4} = \Delta X_{1,2} \cdot \Delta Y_{2,4} \quad (\text{rectangular area}) \quad \text{Equation 28.2}$$

Length components

Length (r) is the distance between the lens' center and the center of ΔS .

It is a length of a spatial line.

$$r^2 = (X_C - X_L)^2 + (Y_C - Y_L)^2 + (Z_C - Z_L)^2 \quad \text{Equation 29}$$

where

(X_C, Y_C, Z_C) are the coordinates of the center point in the small area ΔS .

(X_L, Y_L, Z_L) are the coordinates of the lens' center.

Angles ($\cos(\phi)$ and $\cos(\phi')$)

The spatial angle (ϕ') is between the lens' normal and the line (r), and the spatial angle (ϕ) is between the surface normal and line (r). Usually these two angles are not equal except when the detector is at a vertical position. Figure 13 shows the projective relationship and spatial length and angles.

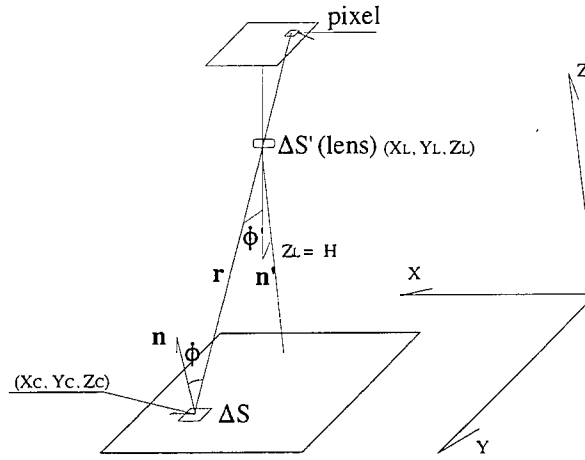


Figure 13. Projective relationship and spatial length and angles.

$$\cos(\phi) = H/r. \quad \text{Equation 30}$$

The formulation for $\cos(\phi')$ is more complex than the one for $\cos(\phi)$. From the analytical geometry, the expression of a sine of the angle between a line and a plane is:

$$\sin(\psi) = \frac{A \cdot h + B \cdot v + C \cdot w}{\sqrt{A^2 + B^2 + C^2} \times \sqrt{h^2 + v^2 + w^2}} \quad \text{Equation 31}$$

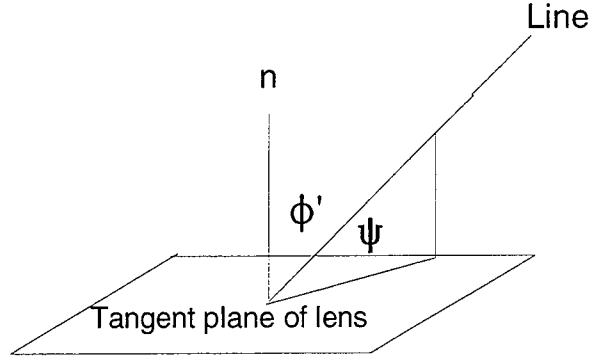


Figure 14. Angle between a line and a plane.

As can be seen in the Figure 14, $\cos(\phi') = \sin(90 - \phi') = \sin(\psi)$. Therefore:

$$\cos(\phi') = \sin(\psi) = \frac{A \cdot h + B \cdot v + C \cdot w}{\sqrt{A^2 + B^2 + C^2} \sqrt{h^2 + v^2 + w^2}} \quad \text{Equation 32}$$

where:

h, v, w are the direction numbers of the projected central line whose length is (r) and A, B, C are the coefficients of a plane equation or the direction number of a normal line of the plane passed through the lens' center point. According to the analytical geometry, the line equation can be determined by:

$$\frac{X - X_L}{X_C - X_L} = \frac{Y - Y_L}{Y_C - Y_L} = \frac{Z - Z_L}{Z_C - Z_L} \quad \text{Equation 33}$$

and:

$$h = X_C - X_L = X_C - 0$$

$$v = Y_C - Y_L = Y_C + H \cdot \tan(t)$$

$$w = Z_C - Z_L = Z_C - H$$

The equation for the normal line (Which is the line between the lens' center and the origin of the object X, Y, Z system) is:

$$\frac{X - 0}{X_L - 0} = \frac{Y - 0}{Y_L - 0} = \frac{Z - 0}{Z_L - 0} \quad \text{Equation 34}$$

i. e.

$$A = X_L = 0,$$

$$B = Y_L = - H \cdot \tan(t),$$

$$C = Z_L = H$$

thus

$$\cos(\phi) = \frac{-H \cdot \tan(t) (Y_C + H \cdot \tan(t)) + H \cdot (Z_C - H)}{\sqrt{(H \cdot \tan(t))^2 + H^2} \times \sqrt{(X_C)^2 + (Y_C + H \cdot \tan(t))^2 + (Z_C - H)^2}}$$

Equation 35

All variables of the simulation model can be determined based on the algorithms discussed above. The simulation program can be written to create a simulated pavement image, the crack percentage can be calculated, and the

influence of the different camera geometries can be analyzed or determined.

The simulated concrete test specimen

In this study, two sample areas were simulated; a large area (5.42 ft × 5.42 ft), and a small area (3.26 ft × 3.26 ft). The simulated cracks designed on the sample area have a V-shaped cross-section with a 60° vertex angle. Crack width varied for the simulated sample areas. The crack varied from zero to about 8.3 inches in width. So the depth of V-shaped cracks varied depending on the crack width. The distribution and relative size of cracks are shown on the Figure 14.1.

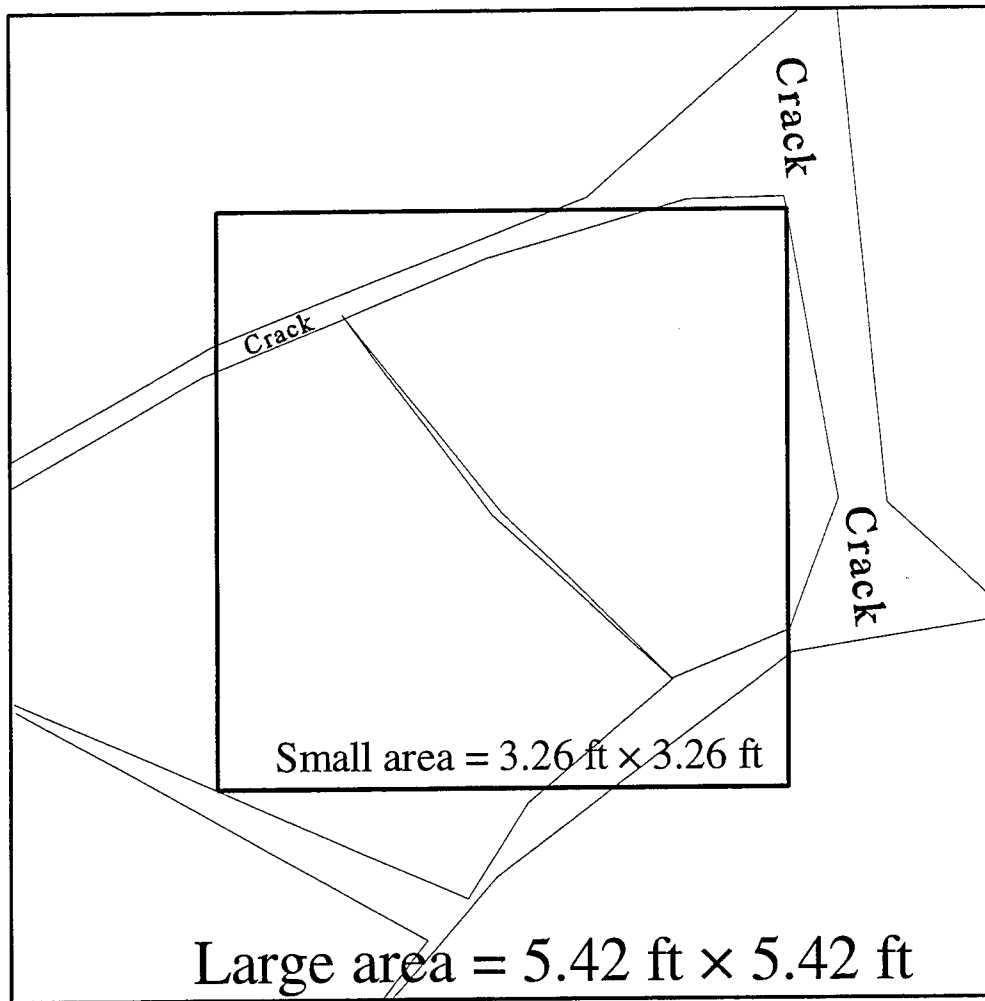


Figure 14.1. Simulated sample areas.

CHAPTER IV PROCEDURE FOR DEVELOPING THE SIMULATION MODEL

Simulation Program

The implementation of the simulation model is accomplished with a simulation program. The results are the simulated data. The simulation programs were written by using the Quickbasic language. The program block diagram is shown as Figure 15. Each of the major program steps will now be described.

Sample pavement area projection onto sensor plane

As mentioned before, the image from a camera is a perspective or central projection. So the image shape of the square sample area is a square when the camera tilt angle is zero and is a trapezoid when the tilt angle is not zero as shown in Figure 16. The data file created in this Step includes the image corner coordinates, the image size, and the camera geometry.

Radiative heat energy calculation for sound pavement element

The energy of each pixel is calculated based on Equation (5) with the emissive power (E) of a defect-free surface. The pixel receiving the energy emitted from the defect-free surface is named the sound pixel. In the same way, the pixel receiving the energy emitted from a crack area is named a crack pixel and a pixel receiving the energy emitted from both a sound area and a crack area is named a boundary pixel. Actually, on the real pavement surface, there are

only two classes of pixels, sound pixels and crack pixels. The procedure for classifying the boundary pixels will be discussed below in the section on classifying the boundary pixel.

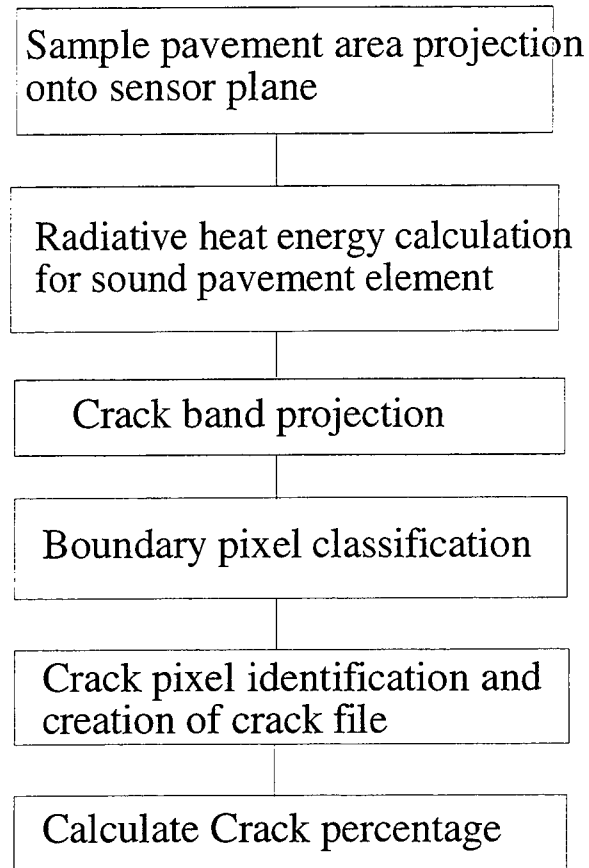


Figure 15. Program block diagram.

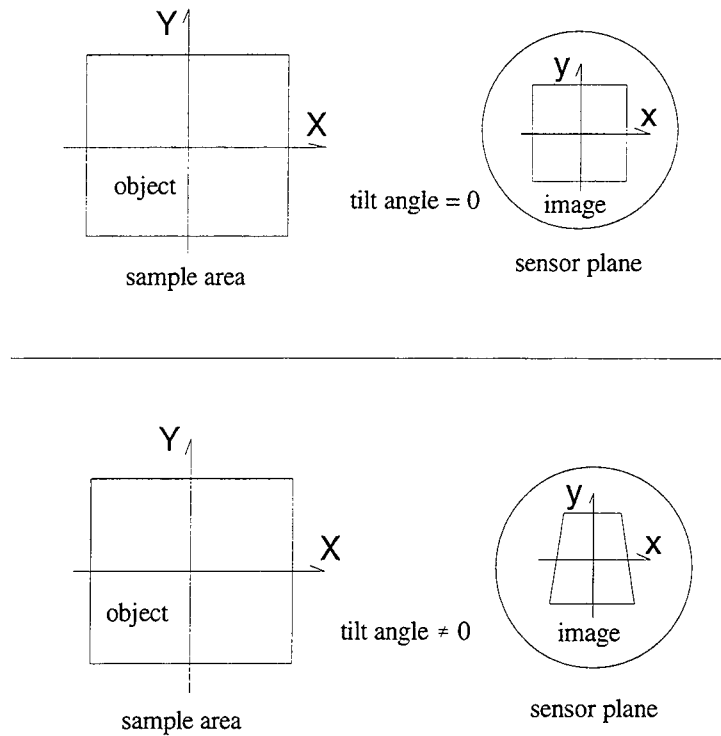


Figure 16. Image size and camera tilt angle.

Crack band projection

In this study, the cracks are considered as consisting of straight line segments (no curve) and each crack includes two boundary lines so it is named the crack band. The crack bands are projected onto the sensor plane with the use of the collinearity equations when the coordinates of two terminal points of each line are fixed or known. When the tilt angle is zero, the shape of the projected band is similar to the one on the pavement surface. When the tilt angle is not zero, the shape of the projected band is not similar to the shape on the pavement surface. Figure 17 shows crack bands on the pavement surface and their projected images on the sensor plane with different tilt angles.

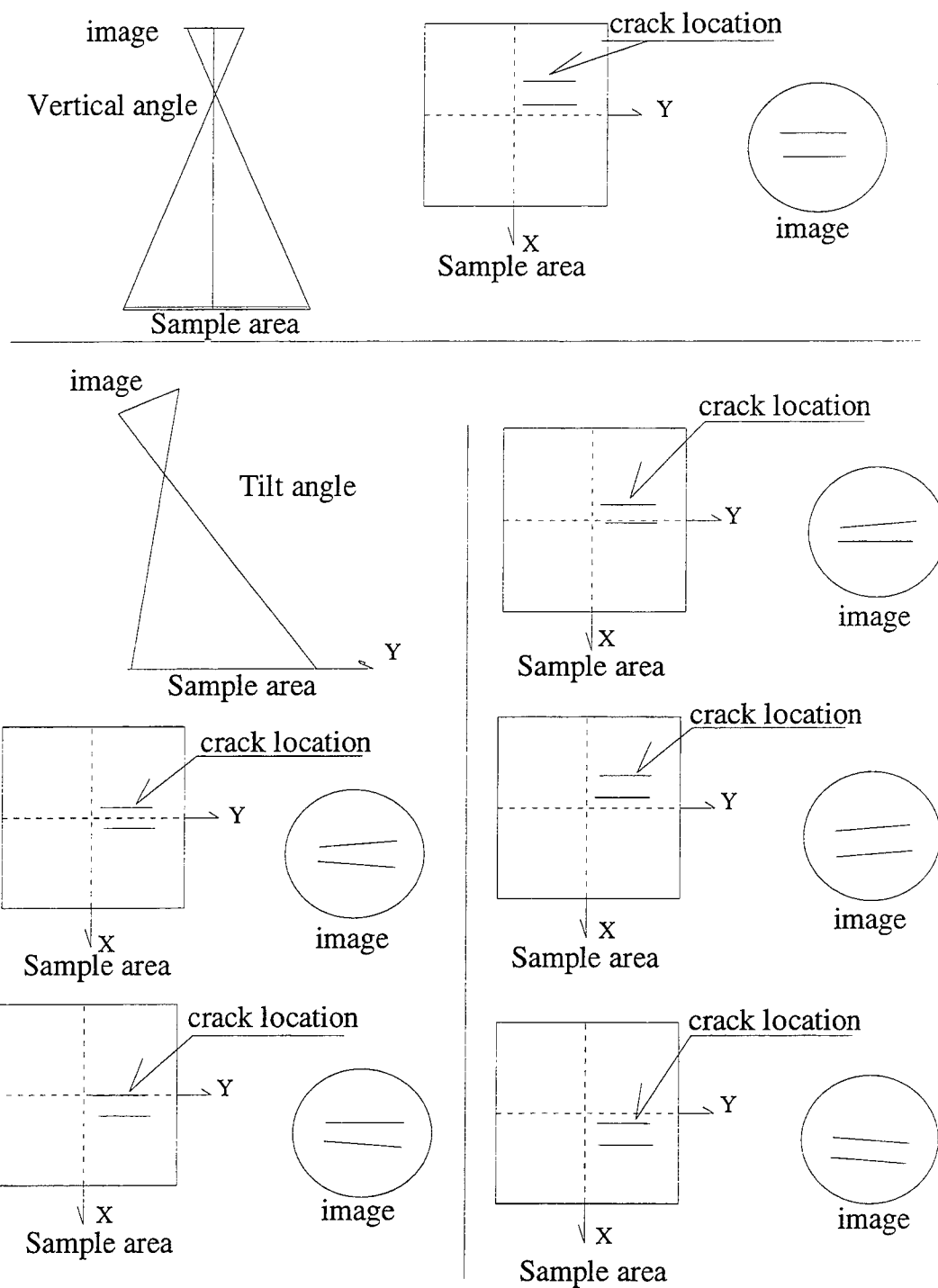


Figure 17. Images of crack bands as projected onto the sensor plane.

Boundary pixel classification

In this step, two problems need to be solved; one is how to locate the boundary pixel (or boundary line) and the other is how to classify the boundary pixel into either a sound pixel or a crack pixel since there are only two categories, sound portion and the crack portion, on a real pavement.

Location of the boundary pixels. The boundary pixels are those passed through by the projected boundary line on the sensor plane. The location of the boundary pixels varies with the slope of the projected boundary line. There are three types of boundary line locations. They are H-type (horizontal position), V-type (vertical position) and D-type (diagonal position) shown in Figure 18(a). If the x-coordinate difference of the two terminal points is less than the pixel size, the boundary pixels are parallel to the y-axis, and if the y-coordinate difference of the two terminal points is less than the pixel size, the boundary pixels are parallel to the x-axis. See Figure 18 (b).

Usually, the locations of boundary pixels include all of the three types of locations. For a projected boundary line, the method of determining the location types is described as follow:

For a given boundary line, the coordinates of its terminal points are known. So the coordinates of the projected terminal points of the boundary line can be determined by using the collinearity Equation 24 and then the linear equation of the line can be determined. Referring to Figure 19, the vertical points (V-points) are where the boundary line intersects the vertical lines of the sensor plane or the vertical edges of pixels and the horizontal points (H-points)

are where the boundary line intersects the horizontal

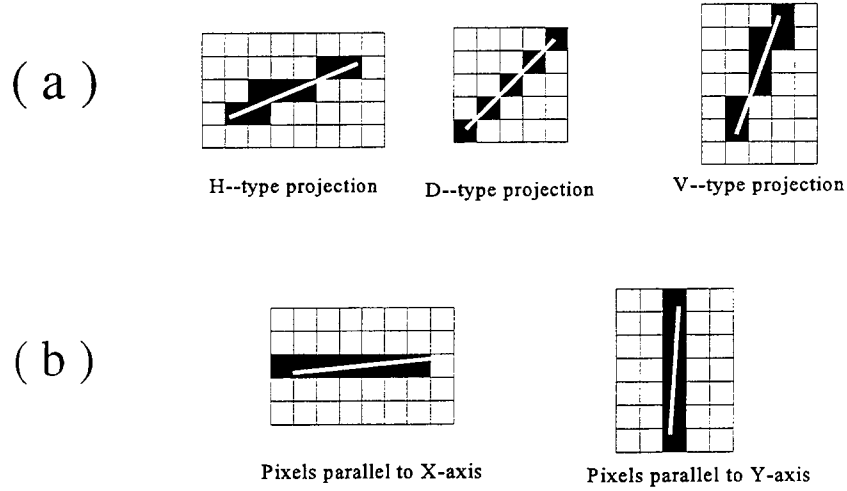


Figure 18. Boundary pixel location.

lines of the sensor plane or the horizontal edges of pixels. The length from the first point (here it is the terminal point A) to the nearest V-point (here it is a point on the line $x = x_i$) is the V-length and the length from the same point (terminal point A) to the nearest H-point (here it is on the line $y = y_i$) is the H-length. If the V-length is greater than the H-length, the pixel (2) is at V-type location i.e. the pixel is located below the former pixel (1). Then shift to the second point (here it is the H-point on the line $y = y_i$) as a new first point to calculate the next V-length and H-length using the same method. This time, the V-length is the distance between second point and the V-point on the line $x = x_i$ and the H-length is that between second point and the point on the line $y = y_{i+1}$. The H-length (see Figure 19) is greater than V-length, so the pixel (3) is at an H-location, i.e. the pixel is located next to the former pixel (2), and so on until all pixel locations of the projected boundary line are determined.

This calculation procedure, actually, is continually solving the linear equations, in which one linear equation presents the projected boundary line and the other is either a vertical line or a horizontal line. For example, when two projected terminal points are determined, the line equation is: $y = ax + b$ where a and b are known. In chapter III, the coordinate system of the sensor plane has been determined so the coordinates of each vertical and horizontal lines on the sensor plane is known. Referring to Figure 19, the calculation proceeds from terminal A to terminal B. Based on the line slope, a terminal point A coordinate, and the pixel size, the nearest horizontal line is $y = y_i$ and the nearest vertical line is $x = x_i$. Then using the line equation $y = ax + b$, the H-point coordinate is ($y_H = y_i$, $x_H = (y_i - b) / a$), the length between A to H-point is $H\text{-length} = ((x_H - x_a)^2 + (y_H - y_a)^2)^{1/2}$, the V-point coordinate is ($x_V = x_i$, $y_V = ax_i + b$), and the length between A to V-point is $V\text{-length} = ((x_V - x_a)^2 + (y_V - y_a)^2)^{1/2}$. Since V-length, as can be seen in Figure 19, is greater than H-length, the boundary pixel is pixel (2) located below the pixel (1). Then shift from the point A to the first H-point as a new terminal point (x_n , y_n) to determine the next V-point and the next H-point. Since the V-point has already been determined, only next H-point is needed to be determined. With the line equation $y = ax + b$ and horizontal line $y = y_{i+1}$, the coordinate is ($y_H = y_{i+1}$, $x_H = (y_{i+1} - b) / a$). The length between the new terminal point and H-point and V-point can be determined with the length equations $((x_H - x_n)^2 + (y_H - y_n)^2)^{1/2}$ and $((x_H - x_n)^2 + (y_H - y_n)^2)^{1/2}$. At this time, the H-length is greater than V-length as can be seen in Figure 19, so the boundary pixel is pixel (3) located next to the pixel (2). This procedure is continued until all boundary pixels are determined.

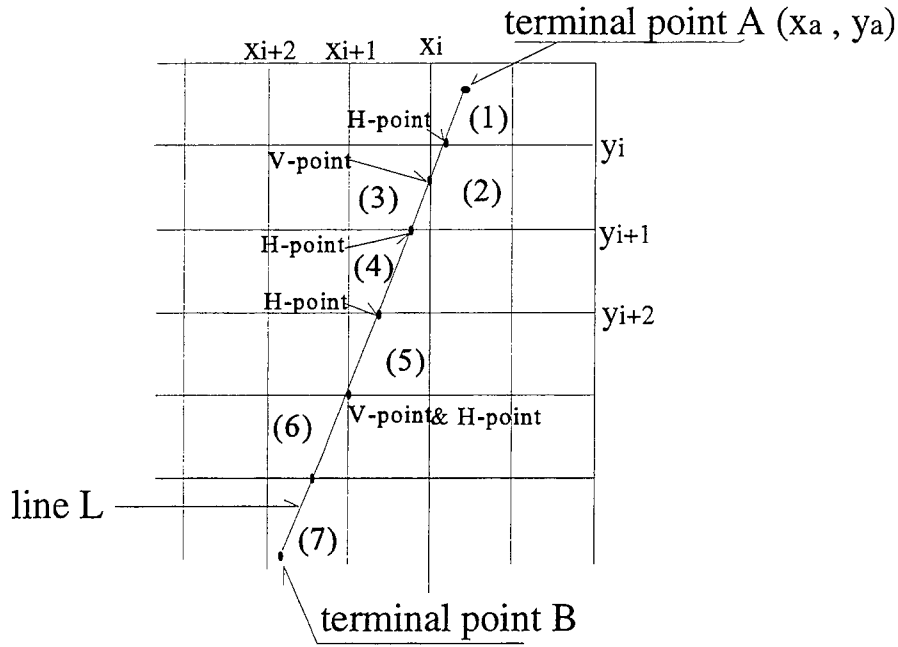


Figure 19. Boundary pixel location.

Classification of the boundary pixel. An energy threshold can be used to classify the boundary pixel as either a crack pixel or a sound pixel. The energy threshold is the minimum energy difference (ΔQ_0) between adjoining pixels for which the infrared sensor will detect a temperature difference. If the energy difference between adjoining pixels is less than (ΔQ_0), then the sensor can't detect the difference. In classifying boundary pixels, if the energy difference between the boundary pixel and its adjacent sound pixel is greater than the energy threshold, the boundary pixel is classified as a crack pixel, otherwise, the boundary pixel is classified as a sound pixel. Since the radiative heat energy is

a function of the temperature, the energy threshold can be expressed by the infrared camera resolution (the temperature unit). In this research, the resolution of the simulated camera is the same as the "INSIGHT 80 SERIES THERMAL IMAGING SYSTEM" whose resolution is 0.2°C, and the simulation temperature is 20°C (about 293°K). When one of the two adjacent pixels has a 0.2°C temperature increase, the energy ratio, using Equation (5) in CHAPTER III, is:

$$\frac{\Delta Q_{T+0.2}}{\Delta Q_T} = \frac{\epsilon \cdot \sigma \cdot (273+20+0.2)^4 \cdot \Delta S' \cdot \Delta S_1 \cdot \cos \phi_1 \cdot \cos \phi' / r_1^2}{\epsilon \cdot \sigma \cdot (273+20)^4 \cdot \Delta S' \cdot \Delta S_2 \cdot \cos \phi_2 \cdot \cos \phi' / r_2^2}$$

Equation 36

Since ΔS_1 and ΔS_2 are finite areas and adjacent to each other, thus

$$\Delta S_1 \cdot \cos(\phi_1) / r_1^2 \approx \Delta S_2 \cdot \cos(\phi_2) / r_2^2$$

then Equation (36) reduces to:

$$\frac{\Delta Q_{T+0.2}}{\Delta Q_T} \approx \frac{(293.2)^4}{(293)^4} \approx 1.003$$

Equation 37

This result shows that, for the simulated camera, the energy threshold is 0.3% of the energy value of a sound pixel or, in other words, when the energy increases by 0.3% (or more) the camera can sense this change.

The boundary pixel shown in Figure 20 consists of two portions. One is P_c projected from the crack area ΔS_c and the other is P_s projected from the sound area ΔS_s . According to the simulation Equation (5), the energy value received by the crack portion P_c is

$$\Delta Q_c = (E_c/\pi) \cdot \Delta S_c \cdot \Delta S' \cdot \cos(\phi_c) \cdot \cos(\phi') / r_c^2 \quad \text{Equation 38}$$

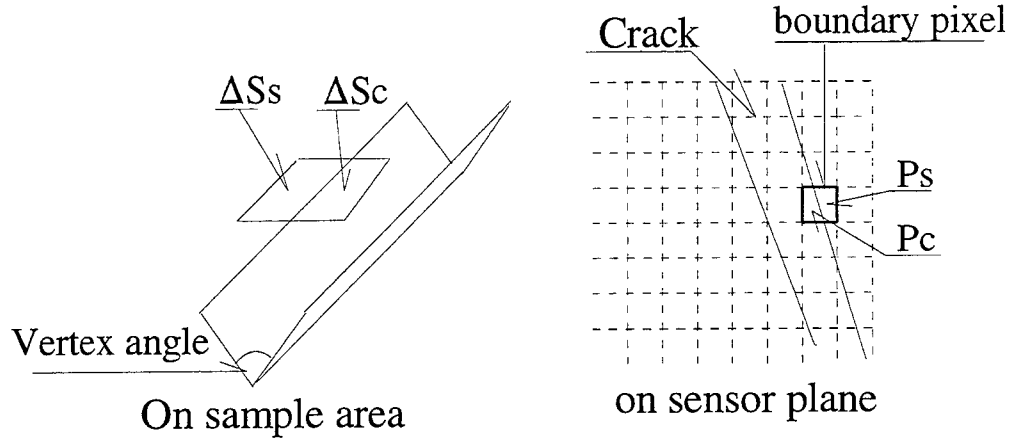


Figure 20. The components of a boundary pixel.

and the energy value received by the sound portion P_s is

$$\Delta Q_s = (E_s/\pi) \cdot \Delta S_s \cdot \Delta S' \cdot \cos(\phi_s) \cdot \cos(\phi') / r_s^2 \quad \text{Equation 39}$$

The energy value of this boundary pixel is

$$\begin{aligned}\Delta Q_b = \Delta Q_c + \Delta Q_s = & (E_c/\pi) \cdot \Delta S_c \cdot \Delta S' \cdot \cos(\phi_c) \cdot \cos(\phi') / r_c^2 + \\ & + (E_s/\pi) \cdot \Delta S_s \cdot \Delta S' \cdot \cos(\phi_s) \cdot \cos(\phi') / r_s^2\end{aligned}$$

Equation 40.1

ΔQ_c and ΔQ_s are the two parts of the ΔQ_b , and ΔS_c and ΔS_s are the two parts of the small area ΔS ($\Delta S_c + \Delta S_s$). The common cosine value and the common length may be used, i. e. , $\cos\phi$ instead of $\cos\phi_c$ and $\cos\phi_s$, and (r) instead of r_c and r_s respectively. Then equation (38) can be deduced as

$$\Delta Q_b = ((E_c) \cdot (\Delta S_c) + (E_s) \cdot (\Delta S_s)) \cdot \Delta S' \cdot \cos(\phi) \cdot \cos(\phi') / r^2 / \pi$$

Equation 40.2

The emissive power value (E_c) (referring to the results and Figures 6, 7, and 8) in the V-shaped crack area is over 1.03 times the emissive power E_s in the sound area. Then equation (40.2) becomes

$$\Delta Q_b = (1.03 \cdot (\Delta S_c) + (\Delta S_s)) \cdot (E_s) \cdot \Delta S' \cdot \cos(\phi) \cdot \cos(\phi') / r^2 / \pi$$

Equation 40.3

The ratio of the ΔQ_b to the energy ΔQ of adjacent sound pixel is

$$\frac{\Delta Q_b}{\Delta Q_0} = \frac{(1.03 \cdot \Delta S_c + \Delta S_s) \cdot E_s \cdot \cos\phi \cdot \cos\phi' / r^2 / \pi}{\Delta S_0 \cdot E_0 \cdot \cos\phi_0 \cdot \cos\phi' / r_0^2 / \pi}$$

Equation 41

Referring to Equations (36) and (37), if this ratio is greater than 1.003, the

boundary pixel will be classified as a crack pixel.

The data files created in this part include the coordinates of boundary pixels and the ratio value.

Crack pixel identification and creation of crack file

Crack pixels are those between the boundary lines and those between a boundary line and the edge of the sample image. See Figure 21.

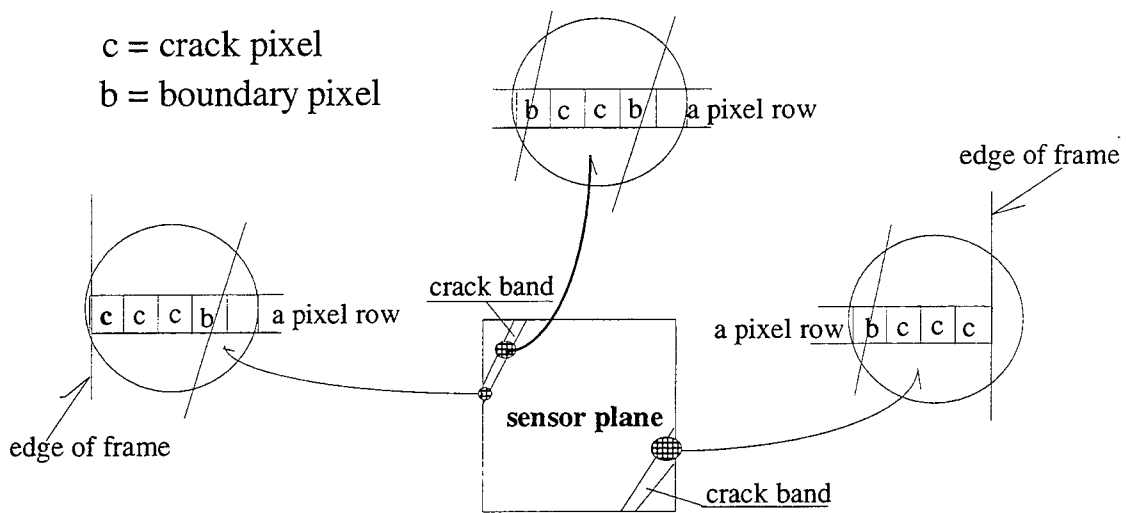


Figure 21. The crack pixel location.

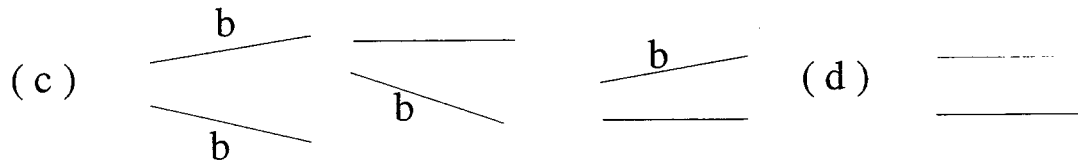
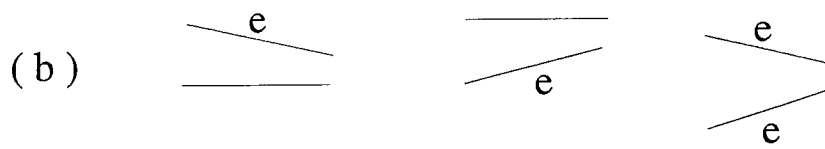
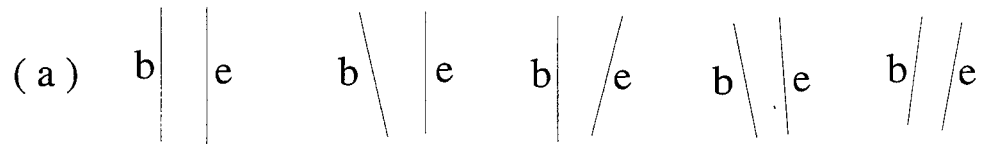
The crack energy value can be calculated by Equation (5) when the emissive power (E_c) in the crack area is known. The E_c is already solved by Equation (11). So the main objective of this part is to determine the position of the crack pixel or, in other words, the coordinates of the crack pixels.

In this simulation program, the coordinates of the crack pixels are determined row by row on the simulated sensor plane from left to right and from the top to the bottom. So for each row, it is necessary to find the beginning pixel that is on the boundary line or the left edge of the image and the ending pixel that is on the boundary line or the right edge of the image. Let the line with the beginning pixels be a beginning line (or b-line) and the line with ending pixels be an ending line (or e-line). The shapes of crack bands are diverse. There is even a simple shape of the crack band such as a straight one along the Y-axis, and the shape on the sensor plane may be straight or oblique depending on the camera geometry (see Figure 17). So there are many shapes of crack bands. Different shapes have different b-lines and e-lines. However, four types of crack bands can be classified based on the b-line and e-line (see Figure 22):

- type one, one b-line and one e-line as shown in Figure 22-(a)
- type two, no b-line and one e-line, or no b-line and two e-lines (as shown in Figure 22-(b))
- type three, two b-lines and no e-line and one b-line as shown in Figure 22-(c).
- type four, no b-line and no e-line as shown in Figure 22-(d)

An example of an image with the various combination of crack shapes is shown in Figure 22-(e).

e = ending-line b = beginning-line



(e) example

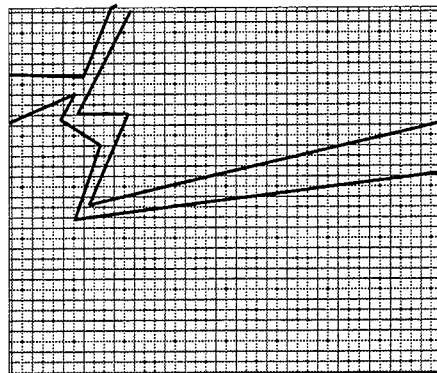


Figure 22. The types of beginning-line and ending-line crack boundaries.

A crack band has two lines with the designed coordinates of their terminal points (object coordinates). The coordinates of the terminal points (image coordinates) of each line on the sensor plane can be calculated with the collinearity Equation 26. According to the image coordinates, the band shaped or line types (see Figure 22) can be determined. As can be seen in Figure 22, the shape of lines of type (a) is different from those of the type (b), (c), and (d) which all have similar line shapes. The x-coordinate of the terminal point of one line in type (a) is less than the coordinates of the terminal points of the other line and the slope angles are between 45° and 135° . The y-coordinate of the terminal point of one line in type (b), (c), or (d) is less than the y-coordinate of the terminal points of the other line and the slope angles are between 135° and 180° or 0° and 45° . For type (a), the beginning line is the line whose terminal point has the smallest x-coordinate. If both lines are horizontal, then the line-type is (d) and there is no beginning line and no ending line.

When both lines of a crack band are non-horizontal and have slopes between 135° and 180° or between 0° and 45° , the lines are either type (b) or type (c) lines. If the lines converge from left to right, i.e., -x to +x, it is a type (b) line and both are ending lines. Whereas, if the lines diverge from left to right, i.e., -x to +x, it is a type (c) line and both are beginning lines.

A type (b) line may also have one horizontal line and the other line non-horizontal. If the slope of the non-horizontal line is positive and the y-coordinates of its end points are less than the y-coordinates of the terminal points

of the horizontal line, then the non-horizontal line is an ending line. If the slope of the non-horizontal line is negative and the y-coordinates of its end points are greater than the y-coordinates of the terminal points of the horizontal line, then the non-horizontal line is an ending line too.

A type (c) line may also have one horizontal line and the other line non-horizontal. If the slope of the non-horizontal line is positive and the y-coordinates of its end points are greater than the y-coordinates of the terminal points of the horizontal line, then the non-horizontal line is a beginning line. If the slope of the non-horizontal line is negative and the y-coordinates of its end points are less than the y-coordinates of the terminal points of the horizontal line, then the non-horizontal line is a beginning line too.

Calculation of the crack percentage

Crack percentage is the ratio of crack pixels to the total pixels of an image frame times 100. The crack pixels include the crack pixels in the crack bands and the crack pixels classified from the boundary pixels. Crack percentage represents the distress extent of the sample surface. The data files created during the simulated procedure may be transformed to an image file which can be manipulated with a commercial software package such as the ERDAS image processing software modules.

CHAPTER V RESULTS AND ANALYSIS

Simulated Data Summary

As mentioned before, there are two simulated sample areas, a "large" one (5.42 feet by 5.42 feet) and a "small" one (3.26 feet by 3.26 feet). A total of 99 images were created for the analysis. There are 66 images of the small area with two camera heights (6' and 8'), three different pixel sizes (0.02 mm, 0.04 mm and 0.06 mm) and eleven tilt angles (0° , 5° , 10° , . . . , 45° , 50°). There are 33 images of the large area with one height (10'), three different pixel sizes (0.02 mm, 0.04 mm and 0.06 mm) and eleven tilt angles (0° , 5° , 10° , . . . , 45° , 50°). So, there are 99 simulated images. The calculated crack percentages are listed in Tables 1, 2, and 3. The information is also shown graphically in Figures 24, 25, and 26.

TABLE 1. Small area (3. 26' by 3. 26'), Height = 6', control crack percentage = 7. 03%
pixel size = 0. 02 mm

<u>CRACK %</u>	<u>CRACK PIXEL/TOTAL PIXEL</u>	<u>TILT ANGLE</u>
7. 104 %	(16505/ 232324)	0
7. 136 %	(16319/ 228692)	5
7. 131 %	(15809/ 221704)	10
7. 215 %	(15154/ 210052)	15
7. 271 %	(14176/ 194926)	20
7. 327 %	(12885/ 175864)	25
7. 410 %	(11456/ 154596)	30
7. 509 %	(9897/ 131800)	35
7. 554 %	(8166/ 108106)	40
7. 693 %	(6536/ 84970)	45
7. 840 %	(5017/ 63996)	50

pixel size = 0. 04 mm

7. 503 %	(4394/ 58564)	0
7. 543 %	(4331/ 57420)	5
7. 543 %	(4199/ 55664)	10
7. 660 %	(4032/ 52634)	15
7. 752 %	(3787/ 48852)	20
7. 767 %	(3431/ 44174)	25
7. 871 %	(3050/ 38748)	30
8. 127 %	(2695/ 33160)	35
8. 308 %	(2268/ 27300)	40
8. 513 %	(1823/ 21414)	45
8. 707 %	(1406/ 16148)	50

pixel size = 0. 06 mm

7. 952 %	(2087/ 26244)	0
8. 067 %	(2072/ 25684)	5
8. 115 %	(2025/ 24954)	10
8. 131 %	(1906/ 23442)	15
8. 241 %	(1810/ 21964)	20
8. 272 %	(1637/ 19790)	25
8. 584 %	(1483/ 17276)	30
8. 804 %	(1301/ 14778)	35
9. 185 %	(1122/ 12216)	40
9. 149 %	(884/ 9662)	45
9. 858 %	(720/ 7304)	50

TABLE 2. Small area (3. 26' by 3. 26'), Height = 8', control crack percentage = 7. 03%
pixel size = 0. 02 mm

<u>CRACK %</u>	<u>CRACK PIXEL/TOTAL PIXEL</u>	<u>TILT ANGLE</u>
7. 179 %	(9828/ 136900)	0
7. 253 %	(9820/ 135382)	5
7. 273 %	(9531/ 131052)	10
7. 328 %	(9091/ 124066)	15
7. 313 %	(8383/ 114638)	20
7. 438 %	(7687/ 103348)	25
7. 517 %	(6804/ 90518)	30
7. 507 %	(5775/ 76926)	35
7. 704 %	(4861/ 63100)	40
7. 723 %	(3826/ 49542)	45
8. 015 %	(2991/ 37324)	50

pixel size = 0. 04 mm

7. 848 %	(2715/ 34596)	0
7. 863 %	(2676/ 34034)	5
7. 874 %	(2594/ 32942)	10
7. 966 %	(2478/ 31108)	15
7. 973 %	(2306/ 28922)	20
8. 184 %	(2135/ 26088)	25
8. 240 %	(1871/ 22706)	30
8. 459 %	(1639/ 19376)	35
8. 710 %	(1392/ 15982)	40
9. 079 %	(1136/ 12512)	45
9. 354 %	(883/ 9440)	50

pixel size = 0. 06 mm

8. 422 %	(1295/ 15376)	0
8. 361 %	(1272/ 15214)	5
8. 495 %	(1247/ 14680)	10
8. 612 %	(1201/ 13946)	15
8. 553 %	(1103/ 12896)	20
9. 240 %	(1068/ 11558)	25
9. 461 %	(965/ 10200)	30
9. 366 %	(809/ 8638)	35
9. 484 %	(677/ 7138)	40
9. 915 %	(557/ 5618)	45
10. 66 %	(458/ 4294)	50

TABLE 3. Large area (5. 42' by 5. 42'), Height = 10', control crack percentage = 11. 49%
pixel size = 0. 02 mm

<u>CRACK %</u>	<u>CRACK PIXEL/TOTAL PIXEL</u>	<u>TILT ANGLE</u>
11. 82 %	(27242/ 230400)	0
11. 74 %	(26843/ 228664)	5
11. 62 %	(25752/ 221670)	10
11. 58 %	(24311/ 210014)	15
11. 51 %	(22438/ 194888)	20
11. 47 %	(20173/ 175836)	25
11. 40 %	(17621/ 154596)	30
11. 66 %	(15359/ 131780)	35
11. 67 %	(12615/ 108090)	40
11. 74 %	(9975/ 84956)	45
11. 89 %	(7605/ 63986)	50

pixel size = 0. 04 mm

12. 58 %	(7245/ 57600)	0
12. 44 %	(7143/ 57408)	5
12. 30 %	(6844/ 55656)	10
12. 24 %	(6384/ 52172)	15
12. 23 %	(5975/ 48844)	20
12. 25 %	(5410/ 44168)	25
12. 27 %	(4753/ 38748)	30
12. 43 %	(4120/ 33154)	35
12. 42 %	(3389/ 27292)	40
12. 79 %	(2738/ 21410)	45
13. 00 %	(2099/ 16146)	50

pixel size = 0. 06 mm

13. 11 %	(3356/ 25600)	0
12. 92 %	(3318/ 25684)	5
12. 75 %	(3181/ 24950)	10
12. 99 %	(3044/ 23440)	15
12. 99 %	(2851/ 21956)	20
12. 96 %	(2564/ 19788)	25
12. 95 %	(2238/ 17276)	30
13. 67 %	(2020/ 14776)	35
14. 32 %	(1749/ 12216)	40
14. 30 %	(1381/ 9660)	45
14. 29 %	(1044/ 7304)	50

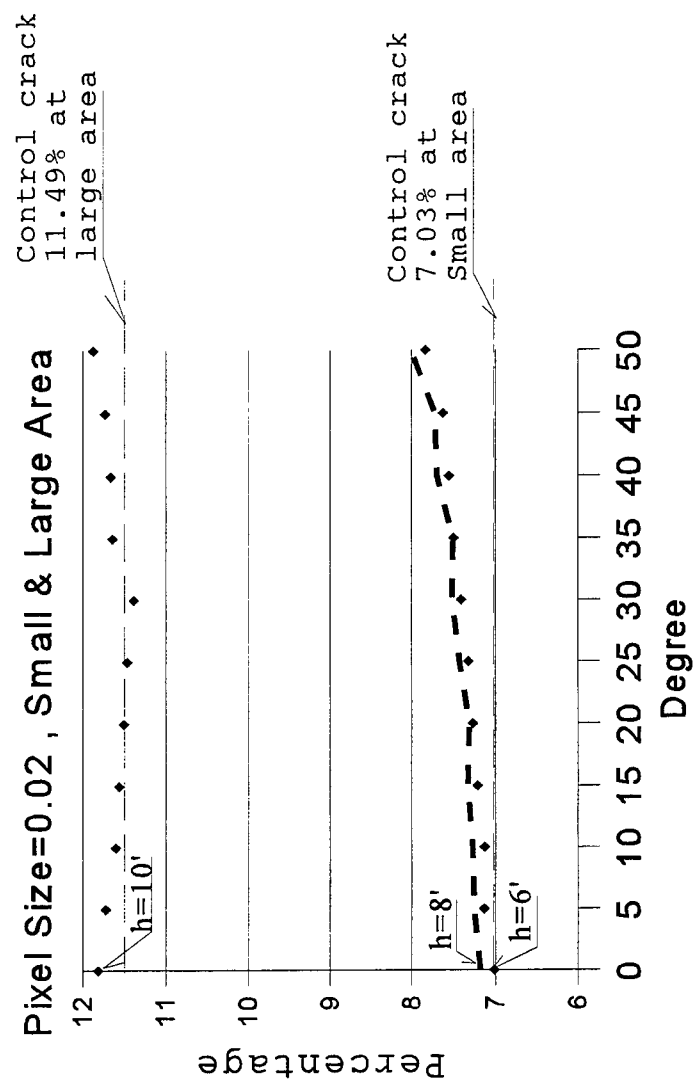


Figure 23. Crack percentage as a function of tilt angle.

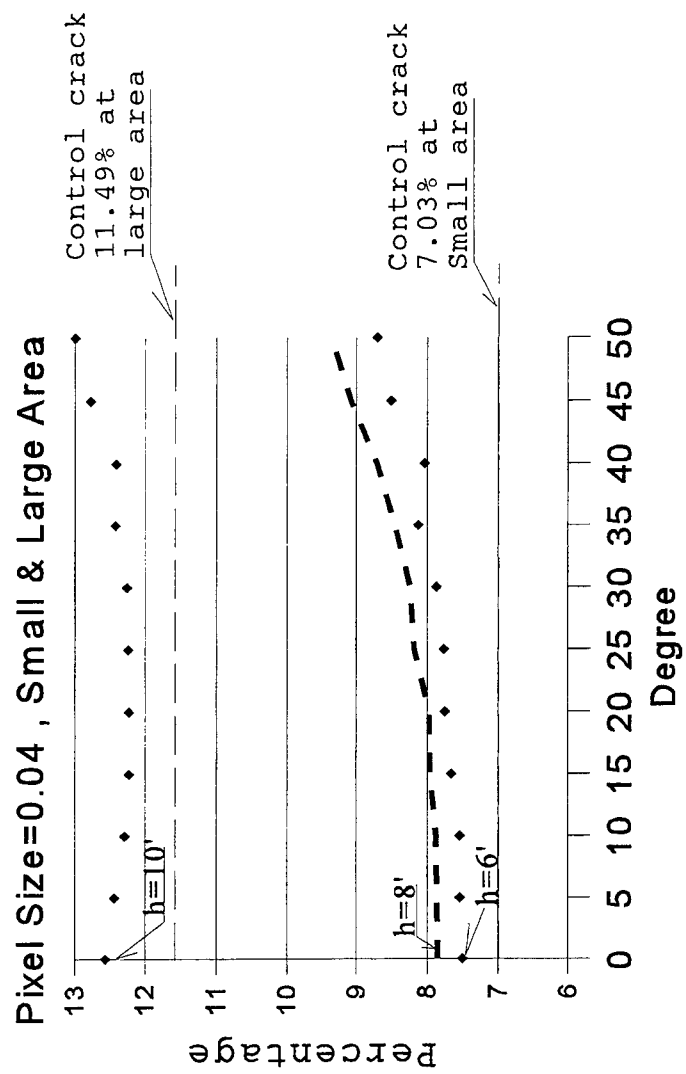


Figure 24. Crack percentage as a function of tilt angle.

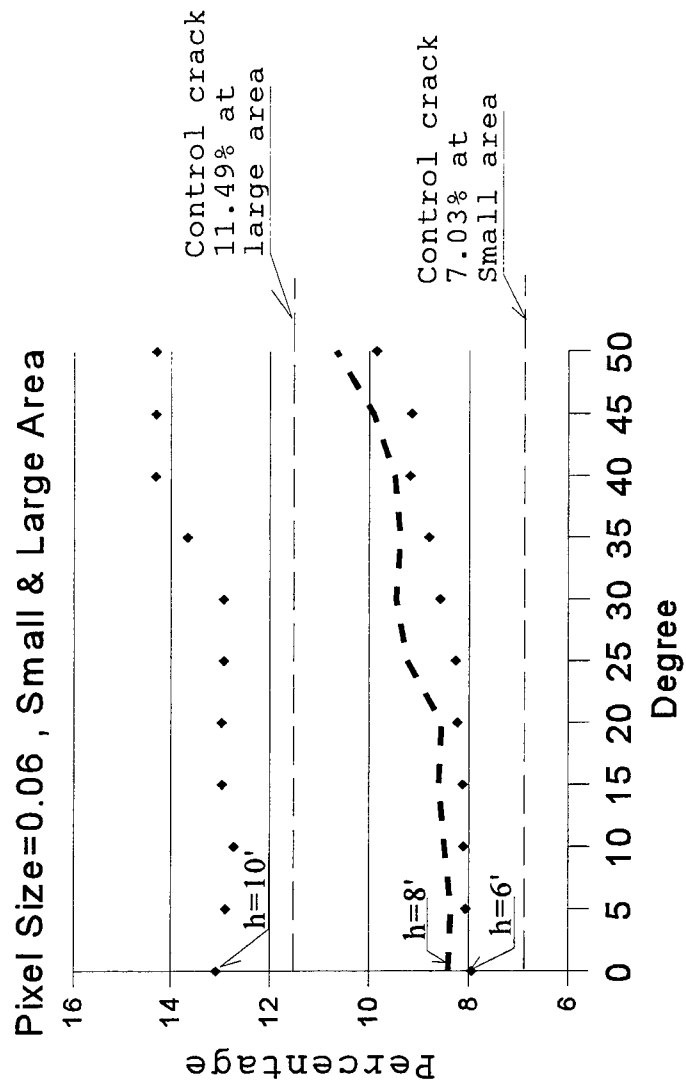


Figure 25. Crack percentage as a function of tilt angle.

Analysis of the results

The control crack percentage is the designed crack percentage, and the calculated crack percentage including those classified from boundary pixels are calculated with the simulation program. The smaller the difference between the control crack percentage and the calculated crack percentage, the better. As can be seen in the tables, the calculated crack percentage of one simulated image is different from that of another. This fact shows that some factors may influence the result of calculating crack percentage. They are the camera geometry (camera height and tilt angle), image location on the sensor plane, pixel size, and the criterion for classifying the boundary pixels. The analysis of these factors follows:

Camera geometry (camera height and tilt angle)

To determine the effect of the camera geometry using the crack percentages, all other factors should be the same or unchanged as comparisons are made. Camera geometry includes a camera height and a camera tilt angle. In this study, the simulated images were used to calculate crack percentages for three different camera heights and eleven different tilt angles for each camera height. If the camera tilt angle has no effect on the calculation of crack percentage, the plot of crack percentage versus tilt angle will be a line parallel with the horizontal or x-axis. See Figure 27 (a). If there is no effect due to the camera height, the plot of crack percentage versus tilt angle will be the same for each of the camera heights. See Figure 27 (b). Finally, if there is no effect due to either camera height or tilt angle, the resulting plot will be a single line parallel

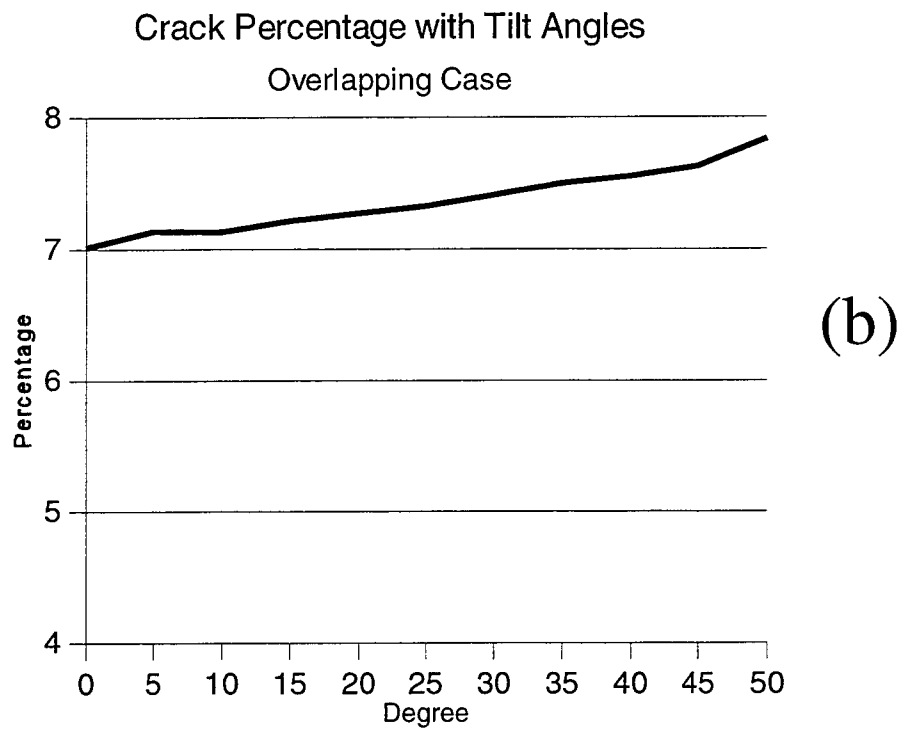
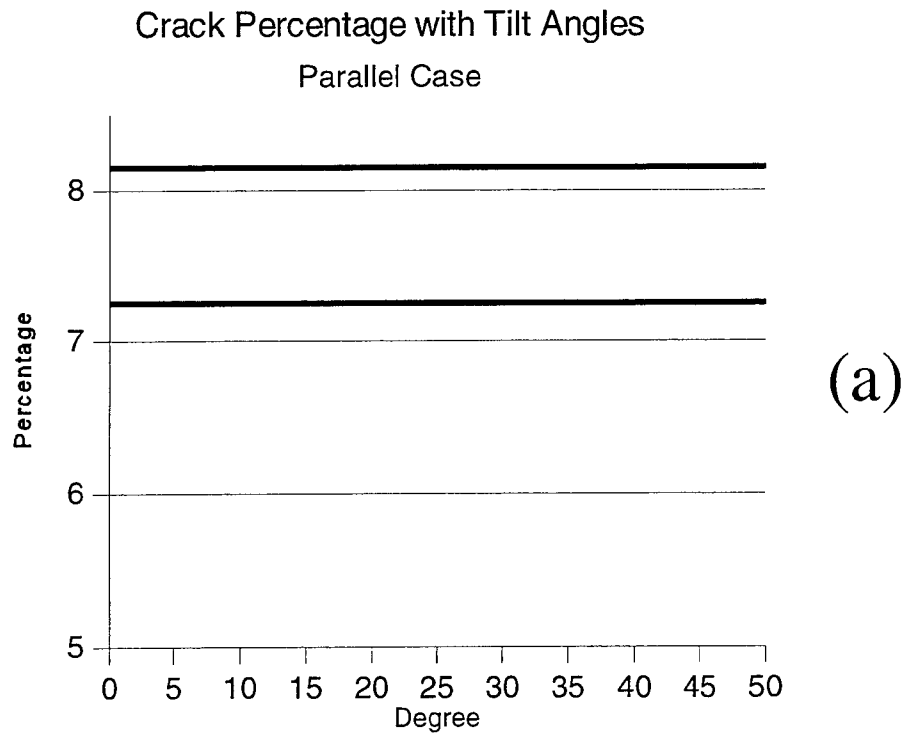


Figure 26. Crack percentage with certain pixel size and same criterion.

with the horizontal axis for all heights.

For the same tilt angle, the difference in crack percentages for two different heights reflects the effect of camera height. Whereas, the difference in crack percentages between a zero tilt angle and another tilt angle at the same camera height will reflect the effect of the camera tilt angle. Furthermore, if the differences in percentages between the zero tilt angle and a given tilt angle for a given height is greater than the difference in percentages between two different heights for the given tilt angle, then the tilt angle factor is more important than height as a factor influencing accuracy. The relationship is reversed if the height differences are greater than the tilt angle differences. A special technique was developed to perform a quantitative analysis utilizing principles discussed above.

Parameters used in the analysis are computed as follows (Refer to Figure 28):

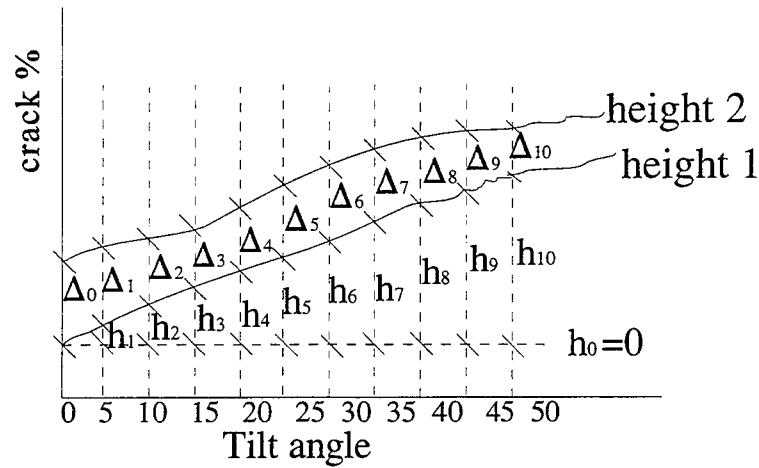


Figure 27. The definition of (h) and (Δ).

h_i = the difference between the crack percentage for each angle and the zero tilt angle at a camera height 1 (tilt angle effect). ($i = 0, 1, 2, \dots, 9, 10$)

Δ_j = the difference between the result of height 1 curve and that of height 2 curve at each tilt angle (height effect). $(j = 0, 1, 2, \dots, 9, 10)$

Thus, $h = \frac{1}{11} \sum_{j=0}^{10} |h_j|$ can reflect the effect of the different tilt angles and $\Delta = \frac{1}{11} \sum_{j=0}^{10} |\Delta_j|$ can reflect the effect of the different heights. If $h = 0$, i. e., the value line of the camera height function is parallel to the x-axis and there is no tilt angle effect. If $\Delta = 0$, i. e., the value lines of two different heights are coincidental with each other, then there is no height change effect. If $h > \Delta$, the tilt angle effect is greater than that of the height effect, and if $\Delta > h$, the height effect is greater than that of the tilt angle effect.

To analyze the simulated data (Tables 1, 2, 3) for determining the effect of camera geometry, the relative values (crack percentage - control crack percentage) were used because the data were from different areas (small and large areas). Using the analysis method described above, the h (for height = 6') and Δ (for height = 8' and height = 10'), h (for height = 8') and Δ (for height = 6' and height = 10'), h (for height = 10') and Δ (for height = 6' and height = 8') were calculated (see Figures 29, 30, and 31). In this study, the boundary pixel classification is the same for all image data. In the cases of different pixel size at Figures 29, 30, and 31, there were 18 pairs of h and Δ in comparison with each other. The comparison results are as follows: 1) for 14 pairs $h > \Delta$ and 2) for 4 pairs $h < \Delta$. So the tilt angle is the major or main factor influencing the determination of the crack percentage and the height is a minor factor influencing the determination of the crack percentage. This result agrees with that of a previous research work (Dean and Kadir, 1992).

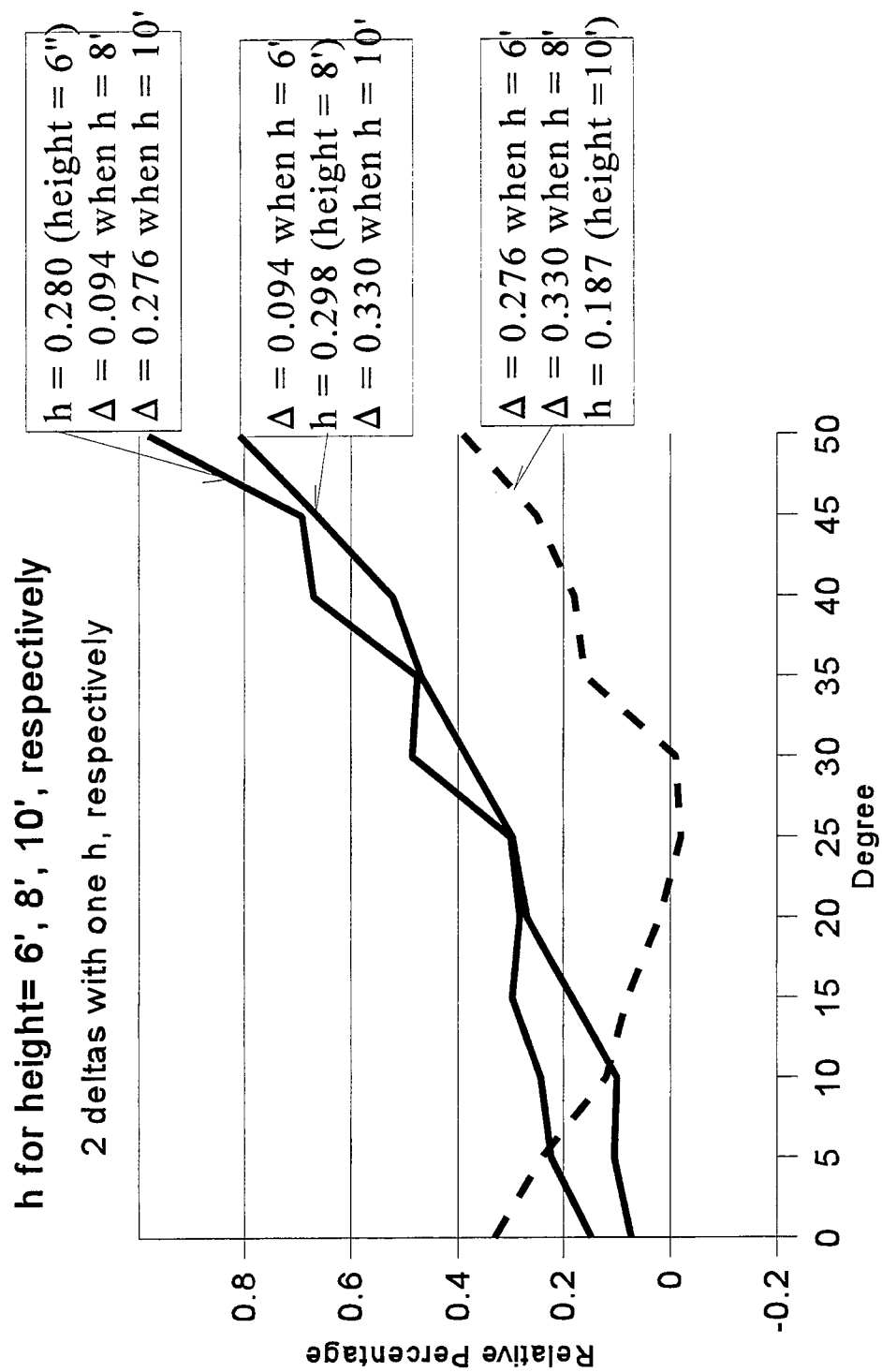


Figure 28. Relative crack percentage (pixel size = 0.02mm).

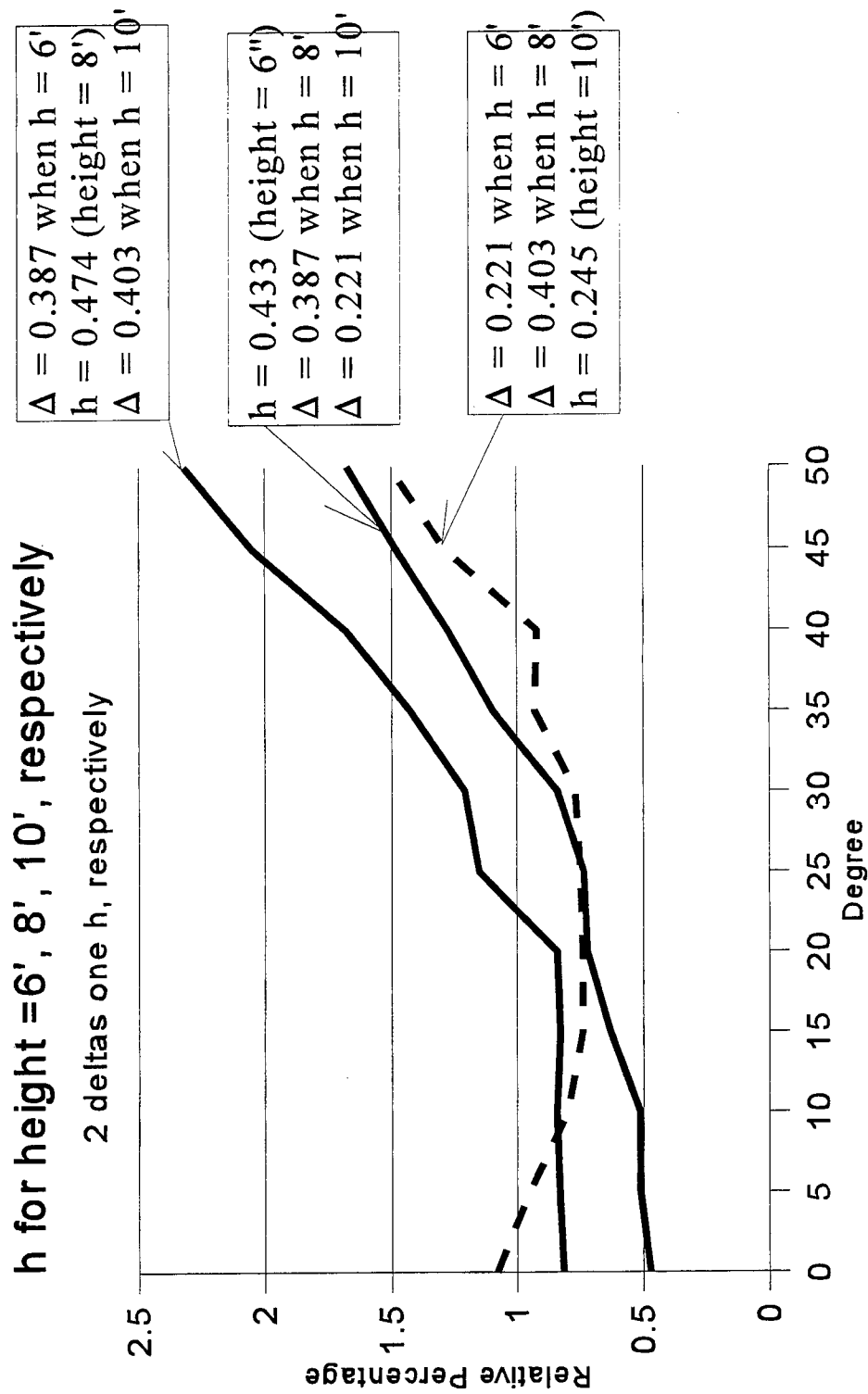


Figure 29. Relative crack percentage (pixel size = 0.04mm).

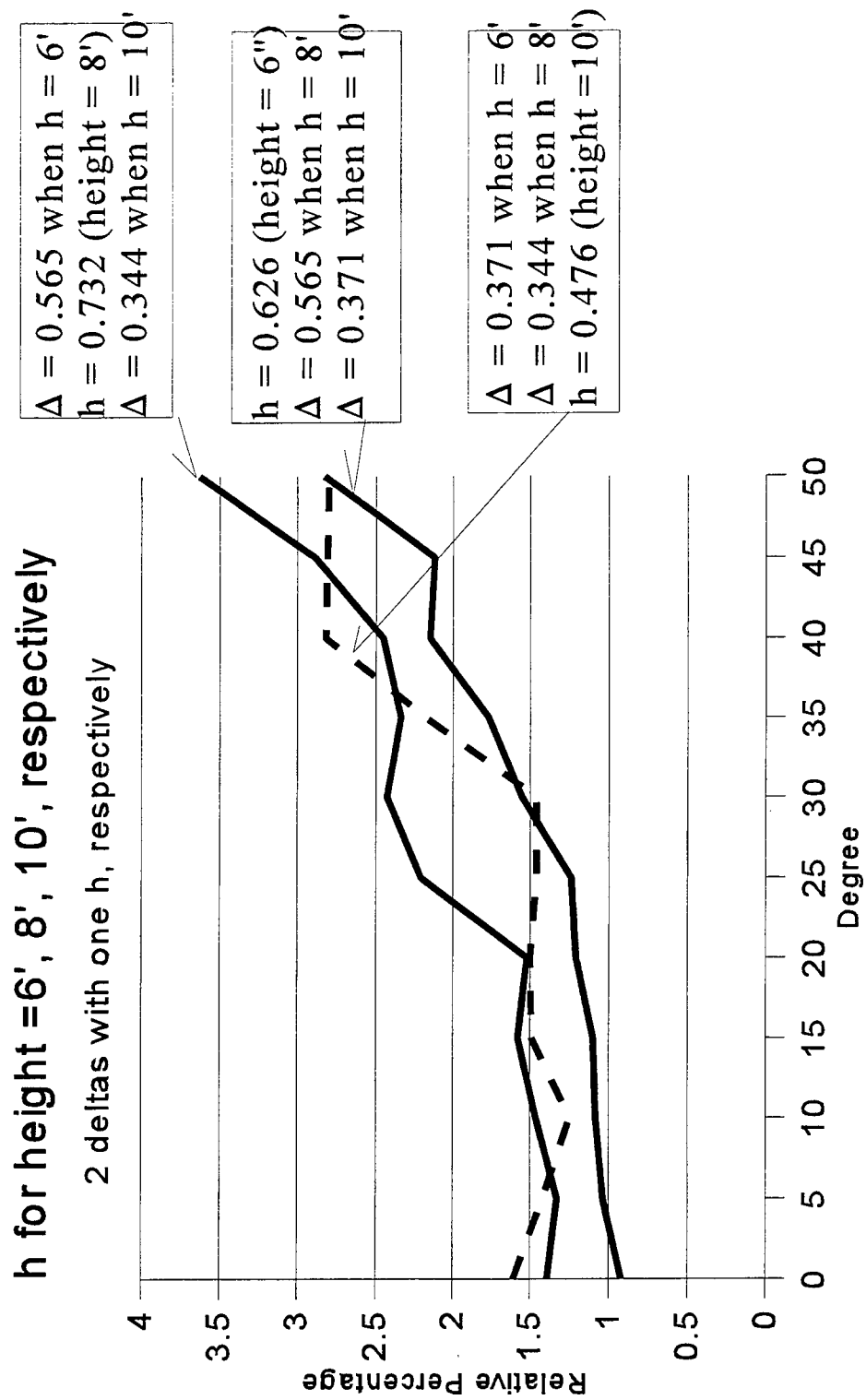


Figure 30. Relative crack percentage (pixel size = 0.06mm).

Crack percentage independent of camera height

Using the simulation model, it can be proven that camera height is not a variable in the energy calculation or, in other words, the energy received by a pixel may not be influenced by the camera height, provided that certain model conditions are met. The process goes as follows:

The infrared energy (ΔQ) received by a pixel can be calculated with Equation (5) in Chapter III, i. e. ,

$$\Delta Q = (E/\pi) \cdot \Delta S \cdot \Delta S' \cdot \cos(\phi) \cdot \cos(\phi') / r^2.$$

where,

ΔS = a differential area covered by a pixel,

$\Delta S'$ = the lens' or aperture area,

ϕ = the angle between normal and the line connecting ΔS ,

ϕ' = the angle between normal and the line connecting $\Delta S'$,

r = the length between ΔS and $\Delta S'$.

These geometry variables (ΔS , $\Delta S'$, ϕ , ϕ' , and r) can be determined with equations from Chapter III. Referring to Equation (27) at Chapter III,

$$X = (Z - H) \frac{x}{\sin t \cdot (y) + \cos t \cdot (-f)}$$

$$Y + H \cdot \tan(t) = (Z - H) \frac{\cos t \cdot (y) - \sin t \cdot (-f)}{\sin t \cdot (y) + \cos t \cdot (-f)}$$

here:

(X, Y, Z) = the object space coordinates on the sample area (so Z = 0),

H = the camera height to be proven independent of ΔQ ,

(x, y) = the pixel coordinates on the sensor plane,

t = the tilt angle,

f = focal length.

Equation (27) may be rewritten as follows:

$$\begin{aligned}
 X &= (Z - H) \frac{x}{\sin t(y) + \cos t(-f)} = (-H) \frac{x}{\sin t(y) + \cos t(-f)} \\
 &= (-H) \cdot F(x, y, t) \\
 Y + H \cdot \tan(t) &= (Z - H) \frac{\cos t(y) - \sin t(-f)}{\sin t(y) + \cos t(-f)} \\
 Y &= (-H) \frac{\cos t(y) - \sin t(-f)}{\sin t(y) + \cos t(-f)} - H \cdot \tan(t) = (-H) \cdot \left(\frac{\cos t(y) - \sin t(-f)}{\sin t(y) + \cos t(-f)} + \tan(t) \right) \\
 &= (-H) \cdot G(x, y, t)
 \end{aligned}$$

So, the area of ΔS is

$$\begin{aligned}
 \Delta S &= 0.5 \cdot ((X_2 - X_1) + (X_4 - X_3)) \cdot (Y_4 - Y_2) \\
 &= 0.5 \cdot (-H) \cdot ((F(x_2, y_2, t) - F(x_1, y_1, t)) + (F(x_4, y_4, t) - F(x_3, y_3, t))) \cdot \\
 &\quad \cdot (-H) \cdot (G(x_4, y_4, t) - G(x_2, y_2, t)) \\
 &= 0.5 \cdot (H^2) \cdot ((F(x_2, y_2, t) - F(x_1, y_1, t)) + (F(x_4, y_4, t) - F(x_3, y_3, t))) \cdot \\
 &\quad \cdot (G(x_4, y_4, t) - G(x_2, y_2, t)) \\
 &= H^2 \cdot S(x_1, y_1, x_2, y_2, x_3, y_3, x_4, y_4, t)
 \end{aligned}$$

where,

$$\begin{aligned}
 S(x_1, y_1, x_2, y_2, x_3, y_3, x_4, y_4, t) &= 0.5 \cdot ((F(x_2, y_2, t) - F(x_1, y_1, t)) + (F(x_4, y_4, t) - \\
 &\quad - F(x_3, y_3, t))) \cdot (G(x_4, y_4, t) - G(x_2, y_2, t))
 \end{aligned}$$

ΔS is the lens area that is independent of the H .

$$\begin{aligned}
 r^2 &= (X_L - X_C)^2 + (Y_L - Y_C)^2 + (Z_L - Z_C)^2 \\
 &= ((-H)F(x_c, y_c, t))^2 + ((-H) \cdot \tan(t) - (-H) \cdot G(x_c, y_c, t))^2 + (-H)^2
 \end{aligned}$$

$$\begin{aligned}
&= (H)^2 \cdot (F(x_c, y_c, t))^2 + (\tan(t) - G(x_c, y_c, t))^2 + 1) \\
&= (H)^2 \cdot R(x_c, y_c, t)
\end{aligned}$$

where,

$$R(x_c, y_c, t) = F(x_c, y_c, t)^2 + (\tan(t) - G(x_c, y_c, t))^2 + 1$$

$$\cos\phi = H / r = H / ((H)^2 \cdot R(x_c, y_c, t))^{1/2}$$

$$= 1 / (R(x_c, y_c, t))^{1/2}$$

$$= \phi(x_c, y_c, t)$$

$$\begin{aligned}
\cos(\phi') &= \frac{-H \cdot \tan(t)(Y_c + H \cdot \tan(t)) + H \cdot (Z_c - H)}{\sqrt{(H \cdot \tan(t))^2 + H^2} \times \sqrt{(X_c)^2 + (Y_c + H \cdot \tan(t))^2 + (Z_c - H)^2}} \\
&= \frac{-H \cdot \tan(t) \cdot (H \cdot G(x_c, y_c, t) + H \cdot \tan(t)) + H \cdot (0 - H)}{H \cdot \sqrt{(\tan(t))^2 + 1} \times \sqrt{(H \cdot F(x_c, y_c, t))^2 + (H \cdot G(x_c, y_c, t) + H \cdot \tan(t))^2 + (0 - H)^2}} \\
&= \frac{-\tan(t) \cdot (G(x_c, y_c, t) + \tan(t)) - 1}{\sqrt{(\tan(t))^2 + 1} \times \sqrt{(F(x_c, y_c, t))^2 + (G(x_c, y_c, t) + \tan(t))^2 + 1}} \\
&= \phi'(x_c, y_c, t)
\end{aligned}$$

Thus:

$$\begin{aligned}
\Delta Q &= (E/\pi) \cdot \Delta S \cdot \Delta S' \cdot \cos(\phi) \cdot \cos(\phi') / r^2. \\
&= (E/\pi) (H^2 \cdot S(x_1, y_1, x_2, y_2, x_3, y_3, x_4, y_4, t)) \cdot \Delta S \cdot \phi'(x_c, y_c, t) \\
&\quad \cdot \phi(x_c, y_c, t) / ((H)^2 \cdot R(x_c, y_c, t)) \\
&= (E/\pi) \cdot S(x_1, y_1, x_2, y_2, x_3, y_3, x_4, y_4, t) \cdot \Delta S \cdot \phi'(x_c, y_c, t) \\
&\quad \cdot \phi(x_c, y_c, t) / R(x_c, y_c, t)
\end{aligned}$$

There is no H variable in the (ΔQ) function. Therefore ΔQ is independent of the H and accuracy should not depend on camera height.

Image location on the sensor plane

The camera tilt angle has a considerable effect on the accuracy of determining the crack percentage. However, the effect of the tilt angle on each sample area is different (refer to Table 1, 2, or 3 or Figure 24, 25, or 26). The results of the small area show that when the camera tilt angle is 0 degree, the simulated crack percentage is close to the control crack percentage, and the results of the large area shows that when the camera tilt angle is not 0 degree, the simulated crack percentage is close to the control crack . The different results between the small sample areas and the large sample area indicates that there may be some other factor influencing the determination of the crack percentage. One possible factor is image position in the image frame. To investigate this factor, an image with a single crack located in different positions, one at the upper position and another at the lower position shown in Figure 32, was designed. Upper and lower positions refer to positions with respect to the tilt angle.

In the Figure 32, the design cracks are of the same area but at different positions

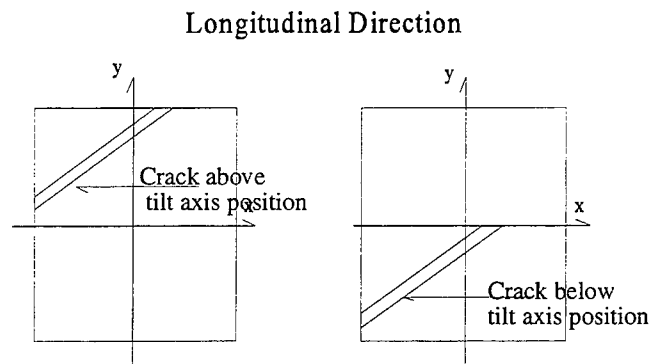


Figure 31. Designed crack in the image frame.

and the calculation results are shown in Table 4 and Figure 33. When the tilt angle is changed from 0 degree to 50 degrees, the crack percentage in the upper area decreases and the crack percentage in lower area increases. This fact shows that the image location of the crack apparently affects the determination of the crack percentage.

TABLE 4. Crack percentage at the designed image frame
(control crack =6. 0%)

Crack at down position		
<u>CRACK %</u>	<u>CRACK PIXEL/TOTAL PIXEL</u>	<u>TILT ANGLE</u>
6. 165 %	(14207/ 230400)	0
6. 358 %	(14542/ 228664)	5
6. 536 %	(14490/ 221670)	10
6. 753 %	(14185/ 210014)	15
6. 913 %	(13475/ 194888)	20
7. 071 %	(12435/ 175836)	25
7. 188 %	(11114/ 154596)	30
7. 276 %	(9590/ 131780)	35
7. 355 %	(7951/ 108090)	40
7. 435 %	(6317/ 84956)	45
7. 450 %	(4770/ 63986)	50
Crack at up position		
6. 140 %	(14158/ 230400)	0
5. 924 %	(13548/ 228664)	5
5. 721 %	(12683/ 221670)	10
5. 526 %	(11607/ 210014)	15
5. 364 %	(10455/ 194888)	20
5. 211 %	(9164/ 175836)	25
5. 108 %	(7898/ 154596)	30
5. 028 %	(6627/ 131780)	35
4. 992 %	(5397/ 108090)	40
5. 004 %	(4252/ 84956)	45
5. 050 %	(3236/ 63986)	50

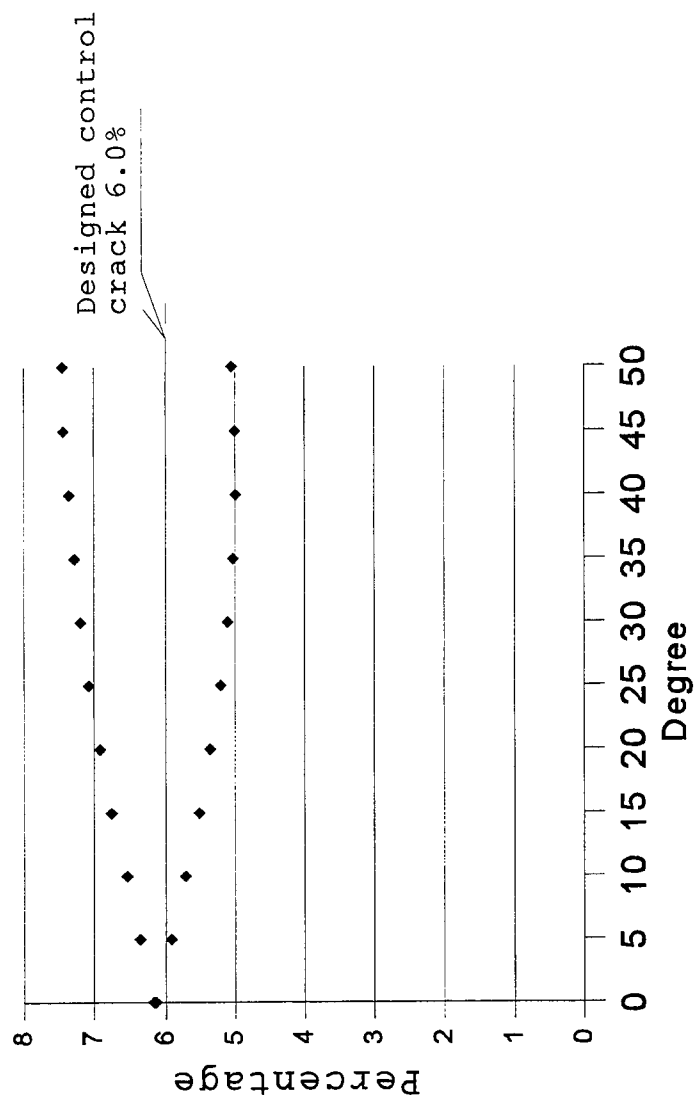


Figure 32. Crack percentage as a function of image location.

Pixel size

In image processing, an analog image that passes through the camera lens and onto the digital sensing array of the sensor plane is quantified into a rectangular grid of intensity values. Each element of this rectangular grid is called a picture element or pixel. The size of the pixel is an indication of the spatial resolution. Each pixel corresponds to a value of the energy intensity over a small rectangular area or a trapezoid area of the image. Intensity quantification occurs when the analog intensity of each pixel is converted into a binary number N bits (i.e., N binary digits) long. Thus each pixel value lies between 0 and 2^N . Often an intensity value of zero is assigned to pixels where the image is darkest (black), while a value of 2^N is assigned to pixels where the image is brightest (white); with intermediate values corresponding to the intermediate shades of grey. The amount of a binary number N refers to the intensity resolution. In this study, the simulated energy intensity is converted to the gray levels from 0 to 255. So the intensity resolution is fixed for all the simulated images. Only the pixel size, i. e. , the spatial resolution is changed to see if it will influence the accuracy of the camera measurement.

Referring to the Tables (1, 2, 3,) and Figures 24, 25, 26 with the same height and tilt angle, it can be seen that when the pixel size increases, the difference of the calculated crack percentage and the control crack percentage increases too. This indicates a degradation in the accuracy of the camera measurement.

The criterion used to classify the boundary pixels

Another factor affecting the accuracy in simulated images is the procedure

used to determine of the boundary pixel classification. A boundary pixel consists of two portions, the crack portion and the sound portion. When a boundary pixel is classified as a crack pixel (or a sound pixel) based on the classification criterion, the result is that the sound portion (or the crack portion) of the boundary pixel will be included in the crack category (or the sound category). In this case, the crack percentage will be greater (or less) than the actual one. Since all boundary pixels in the procedure are not classified as only one class (either sound pixels or crack pixels), or in other words, the classification procedure will increase and decrease the crack percentage so the increase portion will be offset by the decrease portion. Ideally, if the offset were perfect, there would not be any accuracy loss in the classification procedure. However, the offset to the accuracy loss is partly and relative to the classification criterion. So when using software to deal with the infrared thermography, the criterion to classify boundary pixels as either sound or crack pixels should be considered carefully to get a good offset to the accuracy loss.

CHAPTER VI SUMMARY, CONCLUSIONS, AND RECOMMENDATIONS

Summary

This research utilized the simulation method for studying infrared thermography and determining the ability of a camera system to detect pavement cracks. The simulation model developed in this study was based on the radiative heat transfer model. The simulated camera was modeled after the "INSIGHT 80 SERIES THERMAL IMAGING SYSTEM" whose resolution is 0.2°C . The simulated sample areas selected were $5.42\text{ ft} \times 5.42\text{ ft}$ and $3.26\text{ ft} \times 3.26\text{ ft}$. The camera geometric elements of height (6', 8', and 10') and tilt angle (0, 5, 10, ..., 50), were selected for creating the simulated image data. The pixel size, image location at the image frame, and the boundary pixel classification criterion were also considered as factors influencing the accuracy of the infrared thermography system and an analysis of these factors was made.

To determine the parameters of the thermal components and geometric components in the simulation model, some mathematical methods, such as a numerical method for solving the integral equation of the emissive power in the V-shaped crack area and analytical geometry methods, were used.

The simulation programs were developed with use of the Quickbasic language and implemented in the PC computer environment.

Conclusions

In this study, which involved factors such as camera height, tilt angle, pixel size, and the criteria for classifying boundary pixels, 99 simulated images were generated with a simulation program. The results of analyzing these factors indicate that the accuracy in detecting percent area of defects (crack area percentage) is influenced by these factors:

1. The effect of camera height is not significant or the height is independent of the measurement of the radiation heat energy based on the theoretical energy transfer model. So a higher camera height may be used to acquire images. By adopting a higher camera height, larger pavement areas can be scanned and evaluated with no significant loss of accuracy.

2. The effect of the camera tilt angle is significant and this effect is affected by the position of the crack area in the image frame.

3. The effect of the pixel size is significant. The smaller the pixel size, the higher the spatial resolution and the better the image quality.

4. The effect of the criterion of classifying the boundary pixels is significant. So when using software to deal with the infrared thermography, the criterion to classify boundary pixels as either sound or crack pixels should be considered carefully to get a good offset to the accuracy loss.

Recommendations

A practical recommendation from this study is that strict limits on camera height is not required. That is, during pavement inspections, camera height may be adjusted to maximize the extent of the pavement viewed without a loss of accuracy. Recommendations for additional study are made below.

Include more complex crack shapes in the simulation model

In this study, the V-shaped crack bands (segments) are simulated on the sample areas. Although most often cracks are V-shaped beginning at the surface of the pavement, the pavement to be inspected has usually been worn for a long time and the crack shape may be complicated. With the development of a geometry model of the complicated crack shape, the relevant emissive power model must be developed. Usually the main difficulty is to develop the emissive power model.

Explore ways and means of developing a noise model

The simulation model describes the energy exchange between the sample area and the infrared detector. The infrared energy emits from the sample area and goes onto the receiver. Actually, the energy emits not only from the pavement surface, but from other sources as well, such as debris, moisture, air, and other objects. The energy emitted from the pavement surface is called the "signal" and the energy emitted from other sources which disturb the signal received by detector is called the "noise." Apparently, the noise may decrease the accuracy of the inspection system. To further study infrared thermography

by the simulation method, it is recommended that simulation of noise effects be developed.

Further study the simulation method for image classification.

Image classification is a main step in the image processing. In this study, the simulation images have been classified by use of the GISMO module instead of the classification function of the ERDAS software package. This is because the part of image data values representing the sound area are the same as that representing the crack area. These image data can't be classified with the classification function. The key to using GISMO is to generate a defect-free image. The defect-free image may be created by using simulation methods. However, the real infrared images of the concrete samples include not only the signal (object information), but the noise (non- object information) also. So the simulation model for modeling the real defect- free image should consider the noise factor. This will make the simulation model more complex. Based on the radiative heat transfer theory, further study is needed to develop the simulation model with the noise factor.

REFERENCES:

Anonymous, 1985. "Infrared Technique Locates Bridge Deck Delaminations", Road & Bridges, Vol. 23, No.7, pp. 88.

Anonymous, 1990. Proc. Automated Distress Data Collection Equipment Seminar, June 12-15, 1990, Iowa State University, Ames IA, pp. 2-3.

Benson, K. R., Elkins, G. E., Uddin, W., and Hudson, W. R., 1988. "Comparison of Methods and Equipment to Conduct Pavement Distress Surveys", Transportation Research Record, 1196, pp. 40-50.

Bramson, M. A., 1968. Infrared Radiation, New York: Plenum Press.

Bernard, Burton, 1970. ABC's of Infrared, Indianapolis: H. W. Sams.

Brown, J. L., 1990. "The AASHTO Guide for the Design of Pavement Structures: Its Past, Present Research, and Future Improvement," Proc. Automated Distress Data Collection Equipment Seminar, June 12-15, 1990, Iowa State University, Ames IA, pp. 277-284.

Carmichael, R. F. III, 1990. "Pavement Management Systems: Applications and Needs", Proc. Automated Distress Data Collection Equipment Seminar, June 12-15, 1990, Iowa State University, Ames IA, pp. 97-123.

Clarke, D. B, S. B. Harris, A.C. Heitzman, and R. A. Margiotta, 1990. "SHRP Long-Term Pavement Performance Information Management System", Transportation Research Record, 1260, pp. 33-41.

Conner, B., 1990. "Pavement distress Data and its Importance in Pavement Management," Proc. Automated Distress Data Collection Equipment Seminar, June 12-15, 1990, Iowa State University, Ames IA, pp. 285-296.

Copp, R., 1990. "Field test of Three Video distress Recognition Systems: Pavedex, VideoComp, Roadmsn-PCES", Proc. Automated Distress Data Collection Equipment Seminar, June 12-15, 1990, Iowa State University, Ames IA, pp. 239-257.

Dankbar, R., 1990. "Iowa Pavedex Evaluation," Proc. Automated Distress Data Collection Equipment Seminar, June 12-15, 1990, Iowa State University, Ames IA, pp. 195-203.

Darter, M. I., 1990. "Principal Distress Components" Proc. Automated Distress Data Collection Equipment Seminar, June 12-15, 1990, Iowa State University, Ames IA, pp. 195-203.

Dean, R. D. and R. Kadir, 1992. Detection of Highway Pavement Cracks Through Infrared Thermography and Digital Image Processing, Research Report, WVDOH-RP T699-CIDDMOC, Department of Civil Engineering, West Virginia University, Morgantown, WV.

El-Korchi T., and N. Wittels, 1992. "Visual Appearance of Surface Distress in PCC Pavement: I and II Crack Luminance", Transportation Research Record, 1260, pp. 74-90.

Hill, L., "Mn/DOT's Surface Rating: Past, Present, & future, 1990. " Proc. Automated Distress Data Collection Equipment Seminar, June 12-15, 1990, Iowa State University, Ames IA, pp. 83-96.

Hudson, R. D. 1969. Infrared System Engineering, New York: John Wiley & Sons.

Kilareski, W. P., 1990. " Pavement Condition Measuring System Components", Proc. Automated Distress Data Collection Equipment Seminar, June 12-15, 1990, Iowa State University, Ames IA, pp. 125-144.

Kilareski, W. P. and G. Cumberledge, 1990. "Person hour requirements for Visual Evaluation of Pavement Condition", Proc. Automated Distress Data Collection Equipment Seminar, June 12-15, 1990, Iowa State University, Ames IA, pp. 45-60.

Kunz, J. T., and J. M. Eales, 1985. "Evaluation of Bridge Deck Condition by the Use of Thermal Infrared and Ground-Penetrating Radar", Second International Bridge Conference, Pittsburgh, Pa.

Manning D. G. and F. B. Holt, 1986. "The Development of Deck Assessment by Radar and Thermography", Transportation Research Record, 1083, pp. 13-20.

Masliwec T., 1988. " An Experimental and Theoretical Evaluation of IR Thermography for Surveying the condition of Bridge Decks", Journal of Society of Photo-Electronic Engineering, Vol. 934, pp. 19-27.

Maser K. R. and W. M. Kim Roddis , 1990. "Principles of Thermography and Radar for Bridge Deck Assessment", Journal of Transportation Engineering, Vol. 116, No. 5, pp. 583-601.

McGinty, G. P., 1988. Video Cameras: Theory and Servicing, Indianapolis, Indiana: H. W. Sams.

Modest, Michael F., 1993. Radiative Heat transfer, New York: McGraw-Hill, Inc.

Pla G., and M. O. Eberhard, 1992. "Applications of Imaging Technology to the Nondestructive Evaluation of Reinforced Concrete", Proceedings of Nondestructive Evaluation of Civil Structures and Materials, University of Colorado, Boulder, Colorado, pp. 99-112.

Ritchie, S. G., C. I. Yeh, J. P. Mahney, and N. J. Jaksen, 1986. "Development of an Expert System for Pavement Rehabilitation Decision Making", Transportation Research Record, 1070, pp. 96-103.

Schoenberger, G., 1984. " A Pavement Management Information System for Evaluating Pavements and Setting Priorities for Maintenance", Transportation Research Record, 951, pp. 60-63.

Sime, J. M. and D. A. Larsen, 1990. "Objective versus Subjective Pavement-Distress Evaluation Systems", Proc. Automated Distress Data Collection Equipment Seminar, June 12-15, 1990, Iowa State University, Ames IA, pp. 23-43.

Sparrow, E. M., J. L. Gregg, J. V. Szel, and P. Manos, 1961. " Analysis, Results, and Interpretation for Radiation Between Some Simply_Arranged Gray Surfaces", Journal of Heat Transfer, Vol. No. 1, pp. 207-214.

Uzarski, R., 1984. " Managing Better with PAVER", Transportation Research Record, 951, pp. 84-90.

Weil G. J., 1992. " Non-Destructive Testing of Bridge, Highway and Airport Pavements," Proceedings of Nondestructive Evaluation of Civil Structures and Materials, University of Colorado, Boulder, Colorado, pp. 386-393.

Weil G. J., 1989. "Review of the ASTM Standard on IR Testing of Concrete Bridge Decks ", Journal of Society of Photo-Electronic Engineering, Vol. 1094, pp. 32-37.

APPENDIX

BLACKBODY EMISSIVE POWER TABLE

(Source: Modest, 1993)

$n\lambda T$ [$\mu\text{m K}$]	η/nT [cm^{-1}/K]	$E_{b\lambda}/n^3T^5$ [$\text{W}/\text{m}^2\mu\text{m K}^5$]	$E_{b\eta}/nT^3$ [$\text{W}/\text{m}^2\text{cm}^{-1}\text{K}^3$]	$f(n\lambda T)$
1000	10.0000	0.02110×10^{-11}	0.00211×10^{-8}	0.00032
1100	9.0909	0.04846	0.00586	0.00091
1200	8.3333	0.09329	0.01343	0.00213
1300	7.6923	0.15724	0.02657	0.00432
1400	7.1429	0.23932	0.04691	0.00779
1500	6.6667	0.33631	0.07567	0.01285
1600	6.2500	0.44359	0.11356	0.01972
1700	5.8824	0.55603	0.16069	0.02853
1800	5.5556	0.66872	0.21666	0.03934
1900	5.2632	0.77736	0.28063	0.05210
2000	5.0000	0.87858	0.35143	0.06672
2100	4.7619	0.96994	0.42774	0.08305
2200	4.5455	1.04990	0.50815	0.10088
2300	4.3478	1.11768	0.59125	0.12002
2400	4.1667	1.17314	0.67573	0.14025
2500	4.0000	1.21659	0.76037	0.16135
2600	3.8462	1.24868	0.84411	0.18311
2700	3.7037	1.27029	0.92604	0.20535
2800	3.5714	1.28242	1.00542	0.22788
2900	3.4483	1.28612	1.08162	0.25055

$n\lambda T$ [$\mu\text{m K}$]	η/nT [cm^{-1}/K]	$E_{b\lambda}/n^3T^5$ [$\text{W}/\text{m}^2\mu\text{m K}^5$]	$E_{b\eta}/nT^3$ [$\text{W}/\text{m}^2\text{cm}^{-1}\text{K}^3$]	$f(n\lambda T)$
3000	3.3333	1.28245×10^{-11}	1.15420×10^{-8}	0.27322
3100	3.2258	1.27242	1.22280	0.29576
3200	3.1250	1.25702	1.28719	0.31809
3300	3.0303	1.23711	1.34722	0.34009
3400	2.9412	1.21352	1.40283	0.36172
3500	2.8571	1.18695	1.45402	0.38290
3600	2.7778	1.15806	1.50084	0.40359
3700	2.7027	1.12739	1.54340	0.42375
3800	2.6316	1.09544	1.58181	0.44336
3900	2.5641	1.06261	1.61623	0.46240
4000	2.5000	1.02927	1.64683	0.48085
4100	2.4390	0.99571	1.67380	0.49872
4200	2.3810	0.96220	1.69731	0.51599
4300	2.3256	0.92892	1.71758	0.53267
4400	2.2727	0.89607	1.73478	0.54877
4500	2.2222	0.86376	1.74912	0.56429
4600	2.1739	0.83212	1.76078	0.57925
4700	2.1277	0.80124	1.76994	0.59366
4800	2.0833	0.77117	1.77678	0.60753
4900	2.0408	0.74197	1.78146	0.62088
5000	2.0000	0.71366	1.78416	0.63372
5100	1.9608	0.68628	1.78502	0.64606
5200	1.9231	0.65983	1.78419	0.65794
5300	1.8868	0.63432	1.78181	0.66935
5400	1.8519	0.60974	1.77800	0.68033
5500	1.8182	0.58608	1.77288	0.69087
5600	1.7857	0.56332	1.76658	0.70101
5700	1.7544	0.54146	1.75919	0.71076
5800	1.7241	0.52046	1.75081	0.72012
5900	1.6949	0.50030	1.74154	0.72913
6000	1.6667	0.48096	1.73147	0.73778
6100	1.6393	0.46242	1.72066	0.74610
6200	1.6129	0.44464	1.70921	0.75410
6300	1.5873	0.42760	1.69716	0.76180
6400	1.5625	0.41128	1.68460	0.76920
6500	1.5385	0.39564	1.67157	0.77631
6600	1.5152	0.38066	1.65814	0.78316
6700	1.4925	0.36631	1.64435	0.78975
6800	1.4706	0.35256	1.63024	0.79609
6900	1.4493	0.33940	1.61587	0.80219

$n\lambda T$ [$\mu\text{m K}$]	η/nT [cm^{-1}/K]	$E_{b\lambda}/n^3T^5$ [$\text{W}/\text{m}^2\mu\text{m K}^5$]	$E_{b\eta}/nT^3$ [$\text{W}/\text{m}^2\text{cm}^{-1}\text{K}^3$]	$f(n\lambda T)$
7000	1.4286	0.32679×10^{-11}	1.60127×10^{-8}	0.80807
7100	1.4085	0.31471	1.58648	0.81373
7200	1.3889	0.30315	1.57152	0.81918
7300	1.3699	0.29207	1.55644	0.82443
7400	1.3514	0.28146	1.54126	0.82949
7500	1.3333	0.27129	1.52600	0.83436
7600	1.3158	0.26155	1.51069	0.83906
7700	1.2987	0.25221	1.49535	0.84359
7800	1.2821	0.24326	1.48000	0.84796
7900	1.2658	0.23468	1.46465	0.85218
8000	1.2500	0.22646	1.44933	0.85625
8100	1.2346	0.21857	1.43405	0.86017
8200	1.2195	0.21101	1.41882	0.86396
8300	1.2048	0.20375	1.40366	0.86762
8400	1.1905	0.19679	1.38857	0.87115
8500	1.1765	0.19011	1.37357	0.87456
8600	1.1628	0.18370	1.35866	0.87786
8700	1.1494	0.17755	1.34385	0.88105
8800	1.1364	0.17164	1.32916	0.88413
8900	1.1236	0.16596	1.31458	0.88711
9000	1.1111	0.16051	1.30013	0.88999
9100	1.0989	0.15527	1.28580	0.89277
9200	1.0870	0.15024	1.27161	0.89547
9300	1.0753	0.14540	1.25755	0.89807
9400	1.0638	0.14075	1.24363	0.90060
9500	1.0526	0.13627	1.22985	0.90304
9600	1.0417	0.13197	1.21622	0.90541
9700	1.0309	0.12783	1.20274	0.90770
9800	1.0204	0.12384	1.18941	0.90992
9900	1.0101	0.12001	1.17622	0.91207
10,000	1.0000	0.11632	1.16319	0.91415
10,200	0.9804	0.10934	1.13759	0.91813
10,400	0.9615	0.10287	1.11260	0.92188
10,600	0.9434	0.09685	1.08822	0.92540
10,800	0.9259	0.09126	1.06446	0.92872
11,000	0.9091	0.08606	1.04130	0.93184
11,200	0.8929	0.08121	1.01874	0.93479
11,400	0.8772	0.07670	0.99677	0.93758
11,600	0.8621	0.07249	0.97538	0.94021
11,800	0.8475	0.06856	0.95456	0.94270

$n\lambda T$ [$\mu\text{m K}$]	η/nT [cm^{-1}/K]	$E_{b\lambda}/n^3T^5$ [$\text{W}/\text{m}^2\mu\text{m K}^5$]	$E_{b\eta}/nT^3$ [$\text{W}/\text{m}^2\text{cm}^{-1}\text{K}^3$]	$f(n\lambda T)$
12,000	0.8333	0.06488×10^{-11}	0.93430×10^{-8}	0.94505
12,200	0.8197	0.06145	0.91458	0.94728
12,400	0.8065	0.05823	0.89540	0.94939
12,600	0.7937	0.05522	0.87674	0.95139
12,800	0.7813	0.05240	0.85858	0.95329
13,000	0.7692	0.04976	0.84092	0.95509
13,200	0.7576	0.04728	0.82374	0.95680
13,400	0.7463	0.04494	0.80702	0.95843
13,600	0.7353	0.04275	0.79076	0.95998
13,800	0.7246	0.04069	0.77493	0.96145
14,000	0.7143	0.03875	0.75954	0.96285
14,200	0.7042	0.03693	0.74456	0.96418
14,400	0.6944	0.03520	0.72998	0.96546
14,600	0.6849	0.03358	0.71579	0.96667
14,800	0.6757	0.03205	0.70198	0.96783
15,000	0.6667	0.03060	0.68853	0.96893
15,200	0.6579	0.02923	0.67544	0.96999
15,400	0.6494	0.02794	0.66270	0.97100
15,600	0.6410	0.02672	0.65029	0.97196
15,800	0.6329	0.02556	0.63820	0.97288
16,000	0.6250	0.02447	0.62643	0.97377
16,200	0.6173	0.02343	0.61496	0.97461
16,400	0.6098	0.02245	0.60379	0.97542
16,600	0.6024	0.02152	0.59290	0.97620
16,800	0.5952	0.02063	0.58228	0.97694
17,000	0.5882	0.01979	0.57194	0.97765
17,200	0.5814	0.01899	0.56186	0.97834
17,400	0.5747	0.01823	0.55202	0.97899
17,600	0.5682	0.01751	0.54243	0.97962
17,800	0.5618	0.01682	0.53308	0.98023
18,000	0.5556	0.01617	0.52396	0.98081
18,200	0.5495	0.01555	0.51506	0.98137
18,400	0.5435	0.01496	0.50638	0.98191
18,600	0.5376	0.01439	0.49790	0.98243
18,800	0.5319	0.01385	0.48963	0.98293

$n\lambda T$ [$\mu\text{m K}$]	η/nT [cm^{-1}/K]	$E_{b\lambda}/n^3T^5$ [$\text{W}/\text{m}^2\mu\text{m K}^5$]	$E_{b\eta}/nT^3$ [$\text{W}/\text{m}^2\text{cm}^{-1}\text{K}^3$]	$f(n\lambda T)$
19,000	0.5263	0.01334×10^{-11}	0.48155×10^{-8}	0.98340
19,200	0.5208	0.01285	0.47367	0.98387
19,400	0.5155	0.01238	0.46597	0.98431
19,600	0.5102	0.01193	0.45845	0.98474
19,800	0.5051	0.01151	0.45111	0.98515
20,000	0.5000	0.01110	0.44393	0.98555
21,000	0.4762	0.00931	0.41043	0.98735
22,000	0.4545	0.00786	0.38049	0.98886
23,000	0.4348	0.00669	0.35364	0.99014
24,000	0.4167	0.00572	0.32948	0.99123
25,000	0.4000	0.00492	0.30767	0.99217
26,000	0.3846	0.00426	0.28792	0.99297
27,000	0.3704	0.00370	0.26999	0.99367
28,000	0.3571	0.00324	0.25366	0.99429
29,000	0.3448	0.00284	0.23875	0.99482
30,000	0.3333	0.00250	0.22510	0.99529
31,000	0.3226	0.00221	0.21258	0.99571
32,000	0.3125	0.00196	0.20106	0.99607
33,000	0.3030	0.00175	0.19045	0.99640
34,000	0.2941	0.00156	0.18065	0.99669
35,000	0.2857	0.00140	0.17158	0.99695
36,000	0.2778	0.00126	0.16317	0.99719
37,000	0.2703	0.00113	0.15536	0.99740
38,000	0.2632	0.00103	0.14810	0.99759
39,000	0.2564	0.00093	0.14132	0.99776
40,000	0.2500	0.00084	0.13501	0.99792
41,000	0.2439	0.00077	0.12910	0.99806
42,000	0.2381	0.00070	0.12357	0.99819
43,000	0.2326	0.00064	0.11839	0.99831
44,000	0.2273	0.00059	0.11352	0.99842
45,000	0.2222	0.00054	0.10895	0.99851
46,000	0.2174	0.00049	0.10464	0.99861
47,000	0.2128	0.00046	0.10059	0.99869
48,000	0.2083	0.00042	0.09677	0.99877
49,000	0.2041	0.00039	0.09315	0.99884
50,000	0.2000	0.00036	0.08974	0.99890

$n\lambda T$ [$\mu\text{m K}$]	η/nT [cm^{-1}/K]	$E_{b\lambda}/n^3T^5$ [$\text{W}/\text{m}^2\mu\text{m K}^5$]	$E_{b\eta}/nT^3$ [$\text{W}/\text{m}^2\text{cm}^{-1}\text{K}^3$]	$f(n\lambda T)$
19,000	0.5263	0.01334×10^{-11}	0.48155×10^{-8}	0.98340
19,200	0.5208	0.01285	0.47367	0.98387
19,400	0.5155	0.01238	0.46597	0.98431
19,600	0.5102	0.01193	0.45845	0.98474
19,800	0.5051	0.01151	0.45111	0.98515
20,000	0.5000	0.01110	0.44393	0.98555
21,000	0.4762	0.00931	0.41043	0.98735
22,000	0.4545	0.00786	0.38049	0.98886
23,000	0.4348	0.00669	0.35364	0.99014
24,000	0.4167	0.00572	0.32948	0.99123
25,000	0.4000	0.00492	0.30767	0.99217
26,000	0.3846	0.00426	0.28792	0.99297
27,000	0.3704	0.00370	0.26999	0.99367
28,000	0.3571	0.00324	0.25366	0.99429
29,000	0.3448	0.00284	0.23875	0.99482
30,000	0.3333	0.00250	0.22510	0.99529
31,000	0.3226	0.00221	0.21258	0.99571
32,000	0.3125	0.00196	0.20106	0.99607
33,000	0.3030	0.00175	0.19045	0.99640
34,000	0.2941	0.00156	0.18065	0.99669
35,000	0.2857	0.00140	0.17158	0.99695
36,000	0.2778	0.00126	0.16317	0.99719
37,000	0.2703	0.00113	0.15536	0.99740
38,000	0.2632	0.00103	0.14810	0.99759
39,000	0.2564	0.00093	0.14132	0.99776
40,000	0.2500	0.00084	0.13501	0.99792
41,000	0.2439	0.00077	0.12910	0.99806
42,000	0.2381	0.00070	0.12357	0.99819
43,000	0.2326	0.00064	0.11839	0.99831
44,000	0.2273	0.00059	0.11352	0.99842
45,000	0.2222	0.00054	0.10895	0.99851
46,000	0.2174	0.00049	0.10464	0.99861
47,000	0.2128	0.00046	0.10059	0.99869
48,000	0.2083	0.00042	0.09677	0.99877
49,000	0.2041	0.00039	0.09315	0.99884
50,000	0.2000	0.00036	0.08974	0.99890

